



HAL
open science

Combination of $\Delta 47$ and U-Pb dating in tectonic calcite veins unravel the last pulses related to the Pyrenean Shortening (Spain)

Guilhem Hoareau, Nemo Crognier, Brice Lacroix, Charles Aubourg, Nick M.W. Roberts, Nathan Niemi, Mathieu Branellec, Nicolas Beaudoin, Isabel Suárez Ruiz

► To cite this version:

Guilhem Hoareau, Nemo Crognier, Brice Lacroix, Charles Aubourg, Nick M.W. Roberts, et al.. Combination of $\Delta 47$ and U-Pb dating in tectonic calcite veins unravel the last pulses related to the Pyrenean Shortening (Spain). *Earth and Planetary Science Letters*, 2021, 553, pp.116636 - 10.1016/j.epsl.2020.116636 . hal-03492847

HAL Id: hal-03492847

<https://hal.science/hal-03492847>

Submitted on 24 Oct 2022

HAL is a multi-disciplinary open access archive for the deposit and dissemination of scientific research documents, whether they are published or not. The documents may come from teaching and research institutions in France or abroad, or from public or private research centers.

L'archive ouverte pluridisciplinaire **HAL**, est destinée au dépôt et à la diffusion de documents scientifiques de niveau recherche, publiés ou non, émanant des établissements d'enseignement et de recherche français ou étrangers, des laboratoires publics ou privés.



Distributed under a Creative Commons Attribution - NonCommercial 4.0 International License

1 **Combination of $\Delta 47$ and U-Pb dating in tectonic calcite veins unravel the last pulses**
2 **related to the Pyrenean Shortening (Spain)**

3

4 Guilhem Hoareau¹, Nemo Crognier¹, Brice Lacroix², Charles Aubourg¹, Nick M.W. Roberts³,
5 Nathan Niemi⁴, Mathieu Branellec¹, Nicolas Beaudoin¹, Isabel Suárez Ruiz⁵

6

7 1 Université de Pau et des Pays de l'Adour, E2S UPPA, CNRS, TOTAL, LFCR, UMR5150,
8 64000 Pau, France

9 2 Department of Geology, 108 Thompson hall, Kansas State University, Manhattan, KS
10 66506, USA

11 3 NERC Isotope Geosciences Laboratory, British Geological Survey, Nottingham, UK

12 4 Department of Environmental and Earth Science, University of Michigan, USA

13 5 Instituto de Ciencia y Tecnología del Carbono INCAR-CSIC, Oviedo, Spain

14

15 Contact: guilhem.hoareau@univ-pau.fr

16

17

1 **Abstract**

2 Clumped isotopes thermometry ($\Delta 47$) and U-Pb dating of carbonates have been used
3 to elucidate the temperature-time conditions of 10 tectonic calcite veins in the hanging wall of
4 the South Pyrenean Frontal Thrust (Spain), the youngest thrust unit in the south-central
5 Pyrenees. The $\Delta 47$ values indicate precipitation temperatures below $\sim 90^\circ\text{C}$, in agreement with
6 fluid inclusion analyses. 6 veins have been successfully dated, giving ages between 61 and
7 14.5 Ma with all but one value below 24 Ma. On the basis of our new results, we propose that
8 several the studied veins record the end of Pyrenean tectonics in the area during the

9 Burdigalian, possibly up to the Serravalian, younger than estimates based on
10 magnetostratigraphic data from continental syn-tectonic deposits. Calculated $\delta^{18}\text{O}$ values of
11 the precipitating fluid are either very positive, suggesting a local source that has interacted
12 with the host rock, or negative, suggesting the downward incursion of meteoric waters. For
13 undated or pre-burial veins, the $\Delta 47$ values derived from temperature history reordering
14 model (THRM) show that the measured $\Delta 47$ values may have been significantly altered
15 during burial, preventing their use as a reliable thermal or paleohydrological marker.
16 Although applied to a limited number of samples, these results highlight the great potential of
17 the U-Pb/ $\Delta 47$ approach to decipher the history of vein or cement formation and fluid flow in
18 complex tectonic zones, provided that (i) the thermal evolution is known and (ii) the extent of
19 clumped isotope reordering is systematically modelled.

20

21 **Keywords:** Clumped isotopes; carbonate U-Pb geochronology; veins; fractures; Pyrenees

22

23 1. Introduction

24 The links between fracture development and fluid flow in foreland fold and thrust
25 belts has been the subject of active research over the last decades (e.g. Roure et al., 2005 and
26 references therein; Lacroix et al., 2014, 2018; Evans and Fischer, 2012; Beaudoin et al., 2014,
27 2018; Crognier et al., 2018; Cruset et al., 2020). However, in low-temperature systems the
28 precipitation conditions are often obscured by the scarcity of reliable mineral
29 geothermometers and geochronometers, and by the variable impacts of temperature,
30 precipitation rate, and fluid composition, on authigenic mineral composition (e.g. Dromgoole
31 and Walter, 1990; Saulnier et al., 2012; Crognier et al., 2018).

32 Clumped isotope thermometry ideally recovers the temperature of carbonate formation
33 without making assumptions about the composition of precipitating water and / or oxygen

34 composition of another mineral phase, as required for conventional stable isotope
35 thermometry (Ghosh, 2006). The recent development of calibrations to temperatures higher
36 than 100°C (e.g., Bonifacie et al., 2017; Lloyd et al., 2018) has allowed $\Delta 47$ clumped isotope
37 application to the field of fluid migration along tectonic structures, i.e. the Moab fault (e.g.,
38 Bergman et al., 2013; Hodson et al., 2016), the San Andreas Fault Zone (Luetkemeyer et al.,
39 2016), or the Cotiella and Lower Pedraforca thrust faults in the Pyrenees (Lacroix et al., 2018;
40 Cruset et al., 2020). It is also very recently that U-Pb dating of calcite cements by LA-ICPMS
41 has been employed to successfully date brittle faulting and diagenetic cements (e.g., Roberts
42 and Walker 2016; Beaudoin et al., 2018; Mangenot et al., 2018; MacDonald et al., 2019;
43 Cruset et al., 2020). When combined together these techniques may considerably refine the
44 diagenetic and fluid-flow history of sedimentary basins, and increase our understanding of
45 past diagenetic alteration, especially along fault systems (Lawson et al., 2017; Mangenot et
46 al., 2018; MacDonald et al., 2019; Cruset et al., 2020).

47 Here, we focus on the South Pyrenean Frontal Thrust (SPFT), outlined by the Sierras
48 Exteriores (Spain), a complex alignment of folds and thrusts making the most external part of
49 the South-Pyrenean fold and thrust belt. Although its tectonic and sedimentary evolution has
50 been extensively documented (e.g. Turner, 1988, Millán Garrido et al., 1994; Arenas et al.,
51 2001; Oliva-Urcia and Pueyo, 2007; Oliva-Urcia et al., 2016, 2019), only a few studies have
52 focused on the thermal or paleohydrological history of the SPFT (Beaudoin et al., 2015;
53 Labaume et al., 2016). This example is particularly suitable to test whether the combination of
54 $\Delta 47$ clumped isotopes and U-Pb dating of carbonates ($\Delta 47$ /U-Pb thermochronometry) can
55 bring valuable information about the thermal and fluid-flow evolution in complex fault
56 systems.

57 In this contribution, $\Delta 47$ /U-Pb thermochronometry of calcite veins from the SPFT are
58 combined with fracture analysis, fluid-inclusion microthermometry and thermal modeling to

59 define the temperature and timing of vein formation, and to unravel the origin of calcite-
60 precipitating fluid within the tectonic frame of the area.

61

62 **2. Geological Context**

63 The South Pyrenean Frontal Thrust is located at the southern front of the Pyrenees, a
64 double-verging asymmetric fold and thrust belt which developed from the Late Cretaceous to
65 the Early Miocene during the convergence between the Iberian and European plates
66 (Choukroune et al., 1990; Muñoz, 1992; Beaumont et al., 2000; Teixell et al., 2018) (Figure
67 1A). Most of the central and southern part of the Pyrenees is affected by a series of south-
68 verging thrusts and folds (e.g., Labaume et al., 2016 and references therein; Munoz et al.,
69 2002, 2013, 2018). The Axial Zone is made of imbricated thrust units of Paleozoic basement,
70 which connect southward to thrust units affecting Mesozoic to Cenozoic sediments, forming
71 the South Pyrenean Zone (SPZ), which overrides the Ebro foreland basin (Teixell, 1996;
72 Labaume et al., 2016; Teixell et al., 2018). In the west-central Pyrenees, the SPZ corresponds
73 to the Jaca-Pamplona piggyback basin. From north to south, basement thrusts affecting the
74 SPZ along the eastern Jaca basin transverse include the Eaux-Chaudes-Lakora thrust
75 (Ypresian-Bartonian), the Gavarnie thrust (Priabonian-Rupelian), the Broto thrust (Rupelian-
76 Chattian), and the Fiscal and Guarga thrusts (late Rupelian-Aquitania) (Labaume et al.,
77 2016; Oliva-Urcia et al., 2019 and references therein) (Figure 1B). The emergence of the
78 SPFT, forming the Sierras Exteriores in the study zone, was contemporaneous to the Broto
79 and Fiscal-Guarga basement thrusts (~33 – 20 Ma), and accumulated at least 22 km of
80 shortening (Labaume et al., 2016). It subdivided the SPZ in the Jaca–Pamplona basin and the
81 Ebro basin.

82 The Sierras Exteriores consist of a complex WNW-ESE alignment of thrusts, which
83 cross several anticline folds (from the east to the west: Gabardiella, Pico del Aguila, Bentué

84 de Rasal, Santo-Domingo anticlines) (Anastasio, 1987; Millán Garrido et al., 1994, 2000;
85 Arenas et al., 2001) (Figure 1C, D, E). The Gabardiella, Pico del Aguila, Bentué de Rasal and
86 Rasal anticlines formed along with Eaux-Chaudes and Gavarnie thrust activities, and have
87 been interpreted to have formed on oblique ramps of south-verging thrusts (e.g., Pueyo et al.,
88 2002), or as a result of westward propagation of deformation during early Bartonian to
89 Priabonian times (Labaume et al., 2016; Mochales et al., 2012). They have a rough N-S axial
90 orientation, explained by a syn-growth clockwise rotation of up to 40° (Pueyo et al., 2002;
91 Huyghe et al., 2009). The WNW-ESE Santo Domingo anticline formed during Rupelian to
92 Aquitanian times, coeval to the Broto and Fiscal thrusts (Oliva-Urcia et al., 2019). The folds
93 were affected by the emergence of cover thrusts collectively labeled as the Sierras Exteriores
94 thrust by Labaume et al. (2016). These thrusts correspond to the cover equivalent of the
95 Fiscal-Guarga thrusts, and form the SPFT. Although their activity is clearly recognized
96 between the Rupelian and the Aquitanian (e.g., Oliva-Urcia et al., 2019), minor, active
97 compressive tectonics has been proposed to have taken place at least until the Burdigalian, as
98 the uppermost Aquitanian continental deposits of the Uncastillo Formation are folded and
99 thrustured (e.g., the Domingo-Gabardiella thrust system; Millán Garrido et al., 2000; Arenas et
100 al., 2001). In the Pico del Aguila fold, this complex evolution was associated with the
101 development of a polyphase fracture network from the Paleocene to the Oligocene, associated
102 with a multi-stage fluid flow history involving both local waters and the ingress of meteoric
103 water from the surface (Beaudoin et al., 2015).

104 From the early Eocene to the Miocene, the activity of the successive southward-
105 verging thrusts was contemporaneous with deposition of several thousand meters of
106 syntectonic sediments in the Jaca-Pamplona basin, above Triassic to Paleocene pre-tectonic
107 sediments (e.g., Soler-Sampere and Puigdefàbregas, 1970; Carbayo et al., 1972; De Rojas and
108 Latorre, 1972; Samsó et al., 1991; Teixell et al., 1992; Montes and Barnolas, 1992, 2002;

109 Millán Garrido et al., 1994, 2000; Arenas et al., 2001; Oliva-Urcia et al., 2016, 2019; see also
110 references used for thermal modelling in the Supplementary Material) (Figure1B). Based on
111 the references cited above, in the Sierras Exteriores, pre-tectonic sediments include middle
112 Triassic carbonates, upper Triassic shales and evaporites (10-100 m), upper Cretaceous
113 limestones (Adraen-Bona Formation, 50-250 m), and Cretaceous / Paleocene continental
114 deposits (Garumnian Formation, 10-100 m). Overlying syn-folding deposits are marked by
115 significant variations in thickness. They include marine Lutetian platform limestones (Guara
116 Formation; 50-800 m), grading upward into the marine marls of the Arguis-Pamplona
117 Formation (Bartonian; 300-1000 m), and deltaic sandstones (Belsué-Atarès and Yeste-Arrés
118 Formations, Bartonian-Priabonian, 10-200 m). Emersion of the entire Jaca-Pamplona basin
119 during the Priabonian-Chatian was marked by the westward progradation of the Campodarbe
120 conglomerates (~1000-3500 m), uncomfortably overlain by the Uncastillo conglomerates (late
121 Chatian-Aquitania, ~200-500 m).

122 The thermal evolution of the SPFT remains poorly constrained. According to
123 Labaume et al. (2016), the Triassic deposits presently outcropping in the Sierras Exteriores
124 were buried up to ~5 km. Assuming a geothermal gradient of 24 °C/km typical of foreland
125 basins (Allen and Allen, 2013), this would correspond to maximum temperatures of ~140 °C
126 in the studied zone. Such temperature is grossly consistent (i) with the temperatures of ~80-
127 100 °C proposed by Cantarelli (2011) in the Belsué-Atarés and Arguis-Pamplona Formations
128 north of the Rasal anticline (~4 km burial), (ii) with the absence of resetting of apatite fission
129 track ages in Belsué-Atarés sandstones sampled east of the Arguis anticline (Labaume et al.,
130 2016), and (iii) with the low precipitation temperatures of veins sampled in the Pico del
131 Aguila anticline by Beaudoin et al. (2015) ($T < 100^{\circ}\text{C}$).

132

133 **3. Methodology**

134 3.1. Sampling and analytical strategy

135 The initial sampling strategy was intended to increase knowledge of the thermal
136 evolution of the Sierras Exteriores. 17 outcrops of Triassic to Rupelian sedimentary rocks
137 were selected to sample bulk rocks and/or calcite veins (Figure 1B, C, D). 9 bulk rocks
138 appeared suitable for the measurement of vitrinite reflectance (VR) or Rock-Eval (RE) T_{max}
139 values, and were used to build 1D thermal models of the study area. 10 tectonic calcite veins
140 scattered along the Sierras Exteriores were selected to assess fluid temperature conditions
141 both from fluid inclusion data and from $\Delta 47$ clumped isotope analysis (SE1, SE2, SE3, SE4,
142 SE10, SE12, SE13, A21, A22, and A56). Among the veins, three were previously sampled in
143 the Pico del Aguila anticline (A21, A22, and A56, corresponding to sites 436, 439 and 467,
144 respectively, in Beaudoin et al. (2015)). Vein sampling was associated with the analysis of
145 fracture and vein orientations where outcrop conditions permitted (7 veins out of 10: sites
146 SE4, SE10, SE12, SE13, A21, A22, A56), in order to link vein formation to the main tectonic
147 events recorded in the Sierras Exteriores. Given the maximal burial temperatures obtained
148 from VR, RE T_{max} values and thermal modelling ($T > 100^{\circ}\text{C}$; see Results section), U-Pb
149 dating of these calcite veins was then performed to estimate the degree of $\Delta 47$ solid-state
150 reordering which, depending on the thermal history, can lead to erroneous $\Delta 47$ temperatures
151 ($T_{\Delta 47}$) (Lloyd et al., 2018).

152

153 3.2. Analytical methods

154 Petrographic and microstructural characteristics of the veins were studied on polished
155 thick- and thin-sections using optical microscopy and cathodoluminescence (CL). CL images
156 were acquired using an OPEA Cathodyne coupled to a Nikon BH2 microscope at the
157 University of Pau and Pays de l'Adour (LFCR, France). Analytical conditions were with an
158 accelerating voltage of 12.5 kV and an intensity of 200–300 mA.

159 Fluid-inclusion petrography was performed on doubly polished thick sections
160 (100 μm) of the vein samples using a Linkam automatic THMSG600 cooling–heating stage
161 coupled to a Nikon LV-150-ND microscope and a Nikon MK1 camera (University of Pau,
162 LFCR, France). Calibration of the microthermometric stages used synthetic fluid inclusions
163 (FIL, Leoben, Austria), including, (1) pure water (ice melting temperature (T_m) = 0.0 $^{\circ}\text{C}$;
164 critical homogenization temperature (T_h) = 374.1 $^{\circ}\text{C}$), (2) H_2O - CO_2 inclusions (CO_2 melting
165 temperature = -56.6 $^{\circ}\text{C}$; hydrate melting temperature = +9.9 $^{\circ}\text{C}$) and (3) H_2O - NaCl inclusions
166 (eutectic temperature (T_e) = -21.2 $^{\circ}\text{C}$). Accuracy was ± 0.1 $^{\circ}\text{C}$ at temperature between -56.6
167 and +25 $^{\circ}\text{C}$ and ± 2 $^{\circ}\text{C}$ at +374 $^{\circ}\text{C}$. Progressively heating up to T_h was followed by freezing of
168 the inclusions, and their slow heating to tentatively determine their T_e and T_m .

169 Carbon and oxygen isotopes as well as $\Delta 47$ clumped isotopes compositions of the 10
170 vein calcite samples were performed at the University of Michigan. About 6 mg of micro-
171 drilled carbonate powder was loaded into a manual multi-sample rotary carousel. Each
172 sample was then dropped into ~20 ml of anhydrous 105 wt. % phosphoric acid maintained at
173 75 $^{\circ}\text{C}$. Extracted CO_2 was purified following cryogenic procedures (propanol and liquid N_2
174 mixture at -95 $^{\circ}\text{C}$) under vacuum conditions as defined in Ghosh et al. (2006) and Huntington
175 et al. (2009), to remove residual water vapor. CO_2 was then purified to remove any
176 hydrocarbon and halocarbon contaminants by passing through PorapakTM resin at ~ -35 $^{\circ}\text{C}$ for
177 15 min. Finally, purified CO_2 was transferred to a vial for storage for no more than 24 hr
178 before analysis. CO_2 masses 45-49 were measured on a dual-inlet Thermo-Finnigan MAT 253
179 mass spectrometer following the methods of Huntington et al. (2009). $\Delta 47$ values were
180 calculated using the stochastic reference heated gas and equilibrated CO_2 -water (at 25 $^{\circ}\text{C}$)
181 lines produced during the relevant analysis period (March 2014, September 2014 and January
182 2015). Heated gas was produced by heating CO_2 gases of different isotopic compositions in a
183 furnace for 2 hr. Each isotopologue analysis required ~2 1/2 hr of mass spectrometer time to

184 achieve precisions on the order of 10^{-6} for $\Delta 47$ values and each carbonate sample was
185 analyzed at least 3 times in order to reduce uncertainties in derived $\Delta 47$ temperature values.
186 Final temperature values were corrected empirically for acid fractionation factor at 75°C (Guo
187 et al., 2009). $\Delta 47$ results are normalized to the Universal Reference Frame as proposed by
188 Dennis et al. (2011) using $\text{CO}_2\text{-H}_2\text{O}$ equilibration at 25°C and heated CO_2 at 1000°C . $\Delta 47$
189 values are converted into temperatures using the $\Delta 47$ -temperature calibration of Bonifacie et
190 al. (2017).

191 For the host rock samples, O- and C-isotopes analysis was performed at the IStEP
192 (Paris, France), using a Kiel IV Carbonate device connected to a mass spectrometer delta V
193 advantage. About $40\ \mu\text{g}$ of calcite powder was reacted with 104% phosphoric acid at 70°C in
194 individual vials. The CO_2 sample gas produced was purified in an automatic cryogenic
195 system. Instrument calibration was performed using the standard NBS 19 and an in-house
196 standard (Marceau). The analytical precision determined by analysis of NBS 19 was 0.07‰
197 for $\delta^{18}\text{O}$ and 0.03‰ for $\delta^{13}\text{C}$. Carbon and oxygen isotopic composition are reported as relative
198 to Vienna Pee Dee Belemnite (VPDB).

199 U-Pb geochronology via the in-situ LA-ICP-MS method was conducted at the
200 Geochronology & Tracers Facility, NERC Isotope Geosciences Laboratory (Nottingham,
201 UK). The method utilizes a New Wave Research 193UC excimer laser ablation system,
202 coupled to a Nu Instruments Attom single-collector sector-field ICP-MS. The laser
203 parameters used are a $100\ \mu\text{m}$ static spot, fired at 10Hz, with a $\sim 7\text{-}8\ \text{j}\cdot\text{cm}^2$ fluence, for 30
204 seconds of ablation. Normalization uses standard sample bracketing to NIST 614 glass for Pb-
205 Pb ratios, and the WC-1 carbonate reference material for $^{206}\text{Pb}/^{238}\text{U}$ ratios (Roberts et al.,
206 2017). Normalisation is based on the measured/accepted ratio derived from the session-based
207 drift-corrected mean of the primary WC-1 reference material. An additional carbonate
208 material, Duff Brown, was measured in most sessions to provide a control on accuracy and

209 precision. No common lead correction is made; those ages that are deemed robust (based on
210 low MSWD), are determined from lower intercepts on a Tera-Wasserburg plot. Age results
211 are based in lower intercept ages with systematic uncertainties (decay constants, reference
212 material age uncertainty, long-term method reproducibility) propagated. Resulting ages have
213 uncertainties quoted as age \pm x/y, where x is without systematic uncertainties and y is with
214 (see Horstwood et al., 2016). Additional information is available in the Supplementary
215 Material.

216 Vitritine reflectance analyses were performed at the INCAR laboratory (Oviedo,
217 Spain), using reflected white light and an oil immersion objective (50x) in an MPV-Combi-
218 Leitz optical microscope. The petrographic pellets were prepared using a procedure described
219 in the ISO norm (ISO-7404-2, 2009). These pellets are formed by 10-15 g of rock, grounded
220 until a particle size of about 1 mm, blended with a synthetic resin composed by styrene and
221 phthalic anhydride. Rock particles stiffened in the resin in a random statistical orientation.
222 The resulting samples were polished and put for minimum 24 hours in a silica-gel drier before
223 microscopic analysis. All samples were examined under reflected white light. The reflectance
224 was measured in incident white light on vitritine particles of unaltered / unoxidized samples,
225 following the ISO-7404-5 (2009) and ASTM-D7708-11 (2011) norms.

226 Rock-Eval pyrolysis was made using a Rock Eval 6 (VINCI Technologies), at the
227 IStEP (Paris, France), in order to obtain RE Tmax values, which corresponds to the
228 temperature at which the largest quantity of hydrocarbons is released upon cracking.

229

230 **4. Results**

231 4.1. Analysis of fracture and vein orientation

232 The statistical analysis of the fracture network was focused on measurements of joints
233 and veins that exhibit no evidence of shear, at sites SE4, SE10, SE12, and SE13. These data

234 were complemented with previously published data from 3 sites (A21, A22, A56) (Beaudoin
235 et al., 2015). The three stereograms proposed for each site (Figure 2) correspond to the
236 present-day orientations, and to orientations corrected for deformation recorded in the Sierras
237 Exteriores (folding of strata, and regional tilting due to activation of the Guarga thrust, taken
238 as a plane N110°E/30°NE (strike/dip) following Beaudoin et al., 2015). Examples of field
239 photographs of joints and veins are presented in Figure 3A to 3D.

240 For this study, the veins were sampled in stratigraphic levels ranging from the Triassic
241 to the Priabonian. In the Bartonian / Priabonian Arguis-Pampelune marls (sites A21 and A22),
242 most veins are oriented N060°E, and become vertical after unfolding and backtilting. To a
243 lesser extent, N170°E striking fractures are also found. Note that vein A22 was interpreted as
244 a right-lateral fault by Beaudoin et al. (2015). In the Lutetian Guara limestones (sites SE4 and
245 A56), the fracture patterns are similar at both sites, with N110°E preferential orientation,
246 along with a minor N170°E trending set. The latter is orthogonal to bedding in current
247 bedding attitude, whereas the other one is not. In the Cretaceous Adraen Bona formation (site
248 SE12), most fractures are vertical after unfolding and backtilting, trending along the N170°E
249 and N110°E directions. In the middle Triassic (Muschelkalk) beds (sites SE10 and SE13), the
250 fractures are vertical after the same corrections, and 4 trends of fractures striking N060°E,
251 N140°E, N170°E and N040°E are recognized. The N060°E-striking fractures are restricted to
252 the Triassic and Bartonian / Priabonian beds, whereas the N110°E-striking fractures are found
253 both in the Muschelkalk and Eocene limestones. Finally, the N170°E-striking fractures has
254 been measured in all lithologies, and the N140°E-striking fractures are only seen at SE10.

255

256 4.2. Vein petrography

257 Nine of the 10 collected veins consist to either mode I extensional veins or mode I-
258 mode II transtensional shear veins according to the nomenclature of Bons et al. (2012). Only

259 one vein (SE2) corresponds to the mode II (shear vein). Extensional veins (SE1, SE3, SE4,
260 SE10, SE12, SE13, A21 and A56) correspond to mm- to cm-thick veins, filled by granular,
261 blocky or elongated-blocky calcite. Among them, 2 veins (SE1, A56) show evidence of crack-
262 seals events, indicating precipitation coeval to fracture opening. The former one displays
263 multiple crack-seals on the borders and elongated blocky calcite crystals, defining a stretching
264 vein (Bons et al., 2012) (Figure 3E). The latter one is filled by blocky crystals, mixed with
265 pieces and trails of host-rock (Figure 3F). One vein (SE4) is characterized by blocky crystals
266 affected by several stylolites parallel to the vein walls (Figure 4A). The other extensional
267 veins are filled with blocky calcite without evidence of syn-opening precipitation (Figure 4E).

268 The transtensional shear vein (A22) has a thickness of 2.5 cm. It presents a first
269 generation of elongated blocky crystals slightly oblique to the vein walls, corresponding to a
270 first stage of opening (Figure 4B). It is followed by elongated blocky crystals evolving to
271 large blocky crystals towards the center of the vein, corresponding to a second stage of
272 opening and calcite precipitation.

273 The shear vein (SE2) corresponds to a cm-thick body featuring slickenfibres.
274 Microscopically, it comprises stacked (sub)-millimeter thick sheets parallel to the
275 macroscopic vein, formed by the lateral succession of numerous sub-millimetric rhomb-
276 shaped veinlets separated from each other by thin, locally discontinuous, host-rock bands
277 (Figure 4C), similar to the description of Bons et al. (2012; their Fig. 12).

278 Five veins (A56, SE2, SE4, SE12, SE13) present a homogeneous CL, supporting a
279 single precipitation stage or precipitation from waters with similar composition (Machel,
280 2000). They have a dull orange-red color in CL, except SE13 where the CL is extinct. The
281 five other veins present at least two distinct colors. Among these, three veins (A21, SE3,
282 SE10) show concentric CL zoning in the blocky calcite grains, reflecting precipitation under
283 variable redox conditions or variations in precipitation kinetics (Machel, 2000). In A21 and

284 SE3 veins, the CL zonings remain in orange tones (Figure 4E). In SE10 vein, they evolve
285 from orange, to dull and bright yellow, supporting multi-precipitation stages (Figure 4D).
286 Finally, in A22 vein, the CL varies slightly between the 2 cement precipitation stages (dull
287 orange on the borders to brighter orange to the center of the vein) (Figure 4B), whereas for
288 SE1 the fringe of crystals having partially filled some voids have an orange CL brighter than
289 in the rest of vein (Figure 3E).

290

291 4.2. Fluid inclusion petrography and microthermometry

292 All veins show small primary and secondary fluid inclusions (generally below 5 μm),
293 making phase transition temperatures difficult to measure. Only 3 samples (SE2, SE10 and
294 SE12) presented primary two-phase aqueous inclusions with Th in the range 75°C-83°C for
295 sample SE2 (n = 5), 125-185°C for sample SE10 (n = 4) and 79-95°C for sample SE12 (n = 6)
296 (Figure 5A; Table S1). For SE10, most primary fluid inclusions were all liquid, suggesting
297 that the few two-phase inclusions are the results of variable inclusion stretching. The other
298 veins show only single-phase primary inclusions, generally suggesting trapping temperatures
299 below 50°C, or up to ~100°C for very small inclusions (< 3 μm) (Goldstein and Reynolds,
300 1994). The same conclusion applies to the secondary inclusions, which are all liquid in all the
301 veins. No Te and Tm could be measured.

302

303 4.3. Stable and $\Delta 47$ clumped isotopes

304 For the analyzed veins, the $\delta^{18}\text{O}$ and $\delta^{13}\text{C}$ values range between -9.24‰ and +2.69 ‰
305 VPDB, and between -4.47‰ and +1.22‰ VPDB, respectively (Figure 5C; Table S1). Their
306 $\Delta 47$ values range from 0.696‰ to 0.532‰, which can be converted to precipitation
307 temperatures between 21°C and 88 °C (Figure 5B; Table S1). For the three veins presenting

308 two-phase aqueous fluid inclusions, the $T_{\Delta 47}$ values are in good agreement with the
309 homogenization temperatures (Figure 5B).

310 For the host rocks, the isotopic composition range between -2.37‰ and $+2.71\text{‰}$
311 VPDB for $\delta^{13}\text{C}$, and between -6.52‰ and -2.73‰ VPDB for $\delta^{18}\text{O}$ (Figure 5C).

312

313 4.4. Carbonate U-Pb dating

314 Two to 6 transects of spot ablations were performed in 8 of the 10 vein samples
315 selected for U-Pb dating. 6 samples (SE3, SE4, SE10, A21, A22, A56) gave meaningful,
316 accurate ages (that we define as being younger than the depositional age of the enclosing
317 rocks and older than present within 2 sigma uncertainties, and as having MSWD below 2), for
318 at least one transect. Note that sample A21 is included in the successful samples, despite a
319 MSWD of 2.5. The ages obtained range from 60.7 ± 2.9 Ma to 14.4 ± 2.7 Ma (Figure 6; Table
320 S1 and S2). They correspond to one transect (A56, SE10), or from the combination of two
321 transects giving ages similar within uncertainty (A21, A22, SE3, SE4). All veins but one
322 show precipitation ages younger than ~ 24 Ma (23.8 Ma to 11.7 Ma if the age uncertainties are
323 considered).

324

325 4.5. Maturity of organic matter

326 Accurate vitrinite reflectance values could be measured on only 3 samples (1 coal
327 sample in the Triassic (site SE11) and 2 limestone samples in the Cretaceous (site SE12))
328 (Figure 1). The values are $0.32\pm 0.04\%$ (1s) for sample SE11, and $0.34\pm 0.03\%$ and
329 $0.44\pm 0.10\%$ for sample SE12 ($n = 12$) (Figure S2). For Rock-Eval analyses, measurements
330 were performed on 17 powdered samples mostly from the northern part of the study zone.
331 Only 7 samples yielded reliable RE T_{max} values varying from 431 to 443°C (Figure 1B,
332 Table S3).

333

334 **5. Discussion**

335 5.1. Timing of joint and vein emplacement in the SPFT: structural measurements versus U-Pb

336 dating

337 Our novel data of fracture orientation (i.e., joints and veins), combined with existing
338 interpretation of the Pico del Aguila anticline (sites A21, A22 and A56; Beaudoin et al., 2015)
339 allow to propose a sequence of deformation in the Sierras Exteriores. Based on fracture
340 orientations and their link with local fold axis orientation, we first discuss whether the main
341 fractures sets, which comprise the vein analyzed, formed before, during or after folding (see
342 Tavani et al., 2015). We propose that at 4 sites, there are 2 main fracture sets developed
343 before folding, or during early folding: one set trending $\sim N060^\circ E$ comprising fractures at
344 high-angle to bedding (A21, A56, SE10, SE13), and one set trending $\sim N170^\circ E$ (SE10, SE12,
345 SE13). At 2 sites (A22 and SE4), the dominant fracture sets are identified as being late- to
346 post- folding in origin. For site A22, Beaudoin et al. (2015) have shown that the veins result
347 from the reactivation of former joint during Guarga thrusting. For site SE4 (located at the
348 eastern tip of the Santo Domingo anticline), our interpretation is based both on the present-
349 day vertical orientation of the main set, and on its mean strike similar to the fold axis
350 ($\sim N110$).

351 Where U-Pb dating was successful (A21, A22, A56, SE4, SE10), we can refine this
352 interpretation with absolute age constraints. For sites A21 and A56, formation of the
353 $\sim N060^\circ E$ directed fractures (which include the veins dated) during early folding of the Pico
354 del Aguila anticline, as proposed by Beaudoin et al. (2015), would correspond to the
355 Bartonian ($\sim 38-41$ Ma). U-Pb ages show that these fractures actually are cemented with
356 calcite dated to $\sim 14-16$ Ma. For sample A21 (14.7 ± 2.7 Ma), whether the cement is
357 contemporaneous or younger than the opening of the fracture cannot be answered from

358 petrographic observations. However, for sample A56, the young age (16.6 ± 1.1 Ma), added
359 to evidence of syn-tectonic calcite precipitation, suggest that the fracture developed only after
360 the activation of the Guarga thrust (i.e., post-folding), or that the crack-seal may have
361 reactivated an inherited fracture. For site SE10 (Triassic Muschelkalk beds located south-west
362 of the Pico del Aguila anticline), relation to folding of the early \sim N060°E-striking set would
363 lead to interpret it as related to Layer Parallel Shortening (LPS; sensu Bergbauer and Pollard,
364 2004). U-Pb dating (60.7 ± 2.9 Ma) demonstrates that instead, these fractures developed prior
365 to LPS, before regional clockwise rotation, leading us to interpret them as the across-strike set
366 of fractures of the foreland forebulge (sensu Tavani et al., 2015). Accordingly, the other
367 fractures of this site (\sim N170°E-striking) correspond to the along-strike set. For sample A22,
368 the interpretation of a post-folding vein development is compatible with the measured U-Pb
369 age (18.8 ± 5.0 Ma). Finally, for site SE4, the main fracture set likely formed at the end of
370 Santo Domingo folding. According to Oliva-Urcia et al (2019), this fold developed during
371 Chattian-Aquitainian times (\sim 20-27 Ma), slightly older than our U-Pb age of 17.3 ± 3.4 Ma.
372 Petrographic evidence of vertical stylolites in the vein demonstrates clearly that tectonic
373 shortening was still ongoing after vein precipitation, i.e. at least during the Burdigalian.

374 The consequences of the interpretations proposed above are twofold. First, although
375 based only on a limited set of data, the ages obtained by U-Pb dating of calcite veins have
376 bring decisive insights into the sequence of deformation recorded in the SPFT. For some
377 veins (A56 and SE10), absolute age determinations were in contradiction with the
378 interpretations based solely on the study of fracture sets (i.e., younger and older, respectively).
379 We propose that the structural approach to determining relative joint/vein ages in folds should
380 be systematically associated with absolute dating of vein precipitation for greater reliability,
381 as proposed by Beaudoin et al (2018) in the Bighorn Basin (USA). Second, U-Pb dating alone
382 suggests that the SPFT may still have recorded tectonic shortening after 17.3 ± 3.4 Ma at least

383 in the Santo Domingo area, as shown by the results obtained on sample SE4. This age is
384 slightly younger than the minimum age of ~20 Ma proposed by Oliva-Urcia et al. (2019) in
385 their paleomagnetic and tectono-sedimentary study of the Uncastillo Formation at the
386 southern flank of the Santo Domingo anticline. However, it is in accordance with
387 observations that in the same anticline, the uppermost conglomerates of the Uncastillo
388 Formation were folded and thrust by the Domingo-Gabardiella thrust system, suggesting
389 deformation during the Burdigalian (Millán Garrido et al., 2000; Arenas et al., 2001). The
390 other veins that formed after the Aquitanian (A21, A56, SE3) have ages similar to that of
391 sample SE4 within uncertainties, and may also have formed in response to compressive
392 deformation in the SPFT. However, in the absence of petrographic evidence of such
393 deformation, alternative scenarios of joint/vein development may also be considered. For A21
394 and SE3 veins, which do not present evidence of syn-opening precipitation, they include the
395 possibility of a time gap between fracture opening and calcite precipitation, as locally
396 observed in the Bighorn Basin (Beaudoin et al., 2018). For all three samples, joints may have
397 formed earlier (during the Bartonian for A21 and A56) before being reactivated as veins.
398 Finally, for SE3 vein, in the absence of statistical analysis of the fracture network, the
399 development of joint/vein during post-tectonic exhumation cannot be excluded (Engelder,
400 1985; Twiss and Moores, 2006). Nevertheless, our results suggest that fractures can record
401 subtle deformations that would have remained unrevealed with other methods such as the
402 study of tectono-sedimentary relationships. Absolute U-Pb dating of veins provides a robust
403 time frame to these movements, allowing to refine previous interpretations of the tectonic
404 evolution of geologically complex areas such as the SPFT.

405

406 5.2. Thermal evolution of the SPFT and impact on $T\Delta 47$ values

407 *5.2.1. 1D Thermal modelling of the SPFT*

408 Little quantitative data is available on the thermal evolution of the Sierras Exteriores
409 area. To our knowledge only Cantarelli (2011) has proposed maximum burial temperatures of
410 ~80-100°C in the Belsué-Atarés and Arguis-Pamplona Formations, based on vitrinite
411 reflectance and illite crystallinity. To better constrain this thermal evolution, we used our
412 vitrinite reflectance (VR) and RE Tmax values to perform 1D thermal models along 4 virtual
413 stratigraphic wells (San-Felices, Riglos, Nueno and Pico del Aguila from west to east)
414 constructed from compilations of thickness and age of deposition data available in the
415 literature (Figure 7; see the Supplementary Material for details of the approach). The VR
416 measured at the base of each virtual stratigraphic well (0.3 to 0.4%) are abnormally low given
417 thickness of the stratigraphic pile (> 1.5 km before uplift-related erosion), and the VR
418 measured in the Campodarbe Formation (0.3±0.1%) by Izquierdo-Llavall et al (2013). The
419 delay or suppression of vitrinite reflectance has been recognized in various geological
420 contexts and lithologies, and is commonly explained by a hydrogen-rich vitrinite composition
421 or by the development of overpressures (Price and Barker, 1985; Carr, 2000). For this reason,
422 only the thermal models built with the values of RE Tmax have been retained. The RE Tmax
423 values measured in the upper part of the sedimentary columns (431 to 443°C) are all
424 consistent with the onset of the oil window, equivalent to VR of at least ~0.5-0.6% (Lafargue
425 et al., 1998). Using these values in the models results in temperatures of 120 to 140°C at the
426 base of the virtual stratigraphic wells at ~28 Ma, corresponding to the onset of the Fiscal-
427 Guarga thrust (Labaume et al., 2016), and taken as the time of maximum burial before
428 exhumation of the Sierras Exteriores. Such values are equivalent to a VR of ~1.1 to 1.3%
429 (Figure 7). They require adding to the composite logs a substantial thickness of sediments (1
430 to 2 km) that would currently be eroded, leading to an initial thickness of ~2.5 to 3.5 km for
431 the Campodarbe Formation. These values are compatible with those measured on either side
432 of the Sierras Exteriores (Millán Garrido et al., 1995), as are the burial temperature estimates

433 based on RE Tmax values compatible with Cantarelli (2011) estimates and Labaume et al.
434 (2016) reconstructions. Exhumation rates in the southern Pyrenees from the Upper Oligocene
435 are little constrained, notably due to debates about the thickness, spatial extent and timing of
436 the erosion of late- and post-orogenic continental deposits (e.g., Coney et al., 1996; Babault et
437 al., 2005). Therefore, we chose to apply two different, simple exhumation scenarios to the
438 wells. The first scenario implies a temperature of 40°C (1.5 km of burial) at 20 Ma and a
439 current temperature of 15°C at the surface (based on Labaume et al., 2016). In the second
440 scenario, we consider a linear temperature decrease between ~28 Ma and present times. Using
441 these constraints, thermal modelling suggests that all dated veins except SE10 are likely to
442 have precipitated in thermal equilibrium with their host rock (Figure 8).

443

444 *5.2.2. Modelling the effects of solid-state reordering on T Δ 47*

445 It is well known that carbonates can undergo solid-state reordering during diagenesis,
446 resulting in the alteration of their initial Δ 47 values (e.g. Passey and Henkes 2012; Stolper and
447 Eiler 2015; Lawson et al., 2017; Lloyd et al., 2018). Based on an experimental approach,
448 Lloyd et al. (2018) demonstrate that the kinetic of reordering of carbonate can be constrained
449 by the reaction-diffusion model proposed by Stolper and Eiler (2015). This model
450 incorporates both diffusion of isotopes through the crystal lattice and isotope-exchange
451 reactions between adjacent carbonate groups (see Stolper and Eiler 2015 for a complete
452 description). Here, we use a temperature history reordering model (THRM) to explore the
453 kinetic re-ordering of Δ 47 of the studied calcite veins, by integrating the reaction-diffusion
454 model of Stolper and Eiler (2015) (using the numerical code from Lloyd et al., 2018) with the
455 thermal history derived from our 1D thermal modelling, and when available, the measured U-
456 Pb ages.

457 It is worth noting that among the 6 veins dated, the 5 ones having ages younger than
458 23.8 Ma were formed during exhumation, about 9 to 13 Ma after maximum burial (taken as
459 ~28 Ma). According to the 1D thermal model, they did not encompass temperatures higher
460 than 80°C. Experimental and theoretical considerations have shown that clumped isotope
461 reordering is very limited at such low temperatures (< 100°C; e.g., Passey and Henkes 2012;
462 Stolper and Eiler, 2015; Lloyd et al., 2018). For these veins, the T Δ 47 values, which lie
463 below ~80°C, reflect the true precipitation temperature (Table S1). In contrast, the THRM
464 suggests that the vein sample SE10, dated at ~61 Ma, has undergone significant reordering
465 resulting in a measured T Δ 47 higher than the temperature at the time of precipitation, due to
466 burial temperatures higher than 100°C at ~28 Ma. Assuming precipitation temperature
467 identical to the enclosing rocks temperature of ~40°C (as deduced from 1D thermal modelling
468 at 61 Ma), the T Δ 47 values calculated by the THRM can vary between ~45 and ~80°C, if
469 considering the 2 σ uncertainties at the output of the model (Figure 9A). This temperature
470 range is similar to measured T Δ 47 values (Table S1). Considering different temperature
471 conditions of SE10 vein precipitation (for example, 20 and 80°C) results in different
472 reordering pathways, but the final modelled T Δ 47 temperatures can yet be similar to the
473 measured T Δ 47 values. The same conclusion can be drawn for the 4 veins that could not be
474 dated (SE1, SE2, SE12 and SE13). Taking SE2 as an example, temperatures calculated with
475 the THRM fall in the same measured T Δ 47 range (77-97°C) if the veins formed between
476 ~75°C and ~110°C during burial (Figure 9B), or if they formed between ~80°C and ~110°C
477 during exhumation (Figure 9C). The measured T Δ 47 can then be equally explained by
478 precipitation at different temperatures and ages (between ~32 Ma and ~24 Ma). Therefore,
479 reordering modelling shows that modelled present-day Δ 47 temperatures can result from
480 various reordering pathways depending on the age of precipitation (i.e. no significant
481 reordering for late precipitation, or consequent reordering for early precipitation), even for a

482 thermal peak limited in both duration and intensity (< 10 Ma at 100-140°C). In general, the
483 example of the SPFT demonstrates that the use of clumped isotope reordering models based
484 on thermal history should be systematically applied in clumped isotope studies of sedimentary
485 basins, if there is evidence of burial temperature exceeding ~100°C, especially when the ages
486 of carbonates are not precisely constrained.

487

488 5.3. Paleohydrology of the SPFT during late tectonics

489 In order to gather information on the paleohydrology recorded in the Sierras
490 Exteriores during the last tectonic pulses, we derive the $\delta^{18}\text{O}$ values of the waters at the origin
491 of the precipitation of calcite veins ($\delta^{18}\text{O}_w$). To do this, we use both the $\text{T}\Delta 47$ and $\delta^{18}\text{O}$
492 values of calcite veins and the oxygen isotope fractionation factor of Kim and O'Neil (1997).
493 For the reasons mentioned in the previous section, we focus on the 5 samples for which we
494 obtained precise and recent U-Pb ages. For these veins, the $\delta^{18}\text{O}_w$ shows large variations with
495 values ranging from -4.5‰ to +10.3‰ VSMOW (Figure 5D). All the veins considered in this
496 study are hosted within marine sediments. $\delta^{18}\text{O}_w$ values of unaltered marine water source
497 should be ~ -1‰ VSMOW (Zachos et al., 2001). Such values are not recorded in our studied
498 veins suggesting either that (i) the water has been isotopically altered by interaction with the
499 host sediments, or (ii) the veins record water incursions from external reservoirs. The most
500 negative values observed in the SE3 and A56 veins (mean values of -2.6 and -4.5‰,
501 respectively) are compatible with a meteoric source (Longstaffe, 1987), which require
502 infiltration of external water. Considering the young precipitation age of these veins (~16-18
503 Ma), and therefore their formation after the uplift of the area during the Priabonian (Labaume
504 et al., 2016), the incursion of meteoric waters from the surface is not surprising (e.g.,
505 Beaudoin et al., 2015; Roure et al., 2005; Lacroix et al., 2014). The very low $\text{T}\Delta 47$ obtained
506 for SE3 vein, which requires the incursion of water colder than the enclosing rock, further

507 reinforces this interpretation. The 3 other veins which formed after 25 Ma (SE4, A21, A22)
508 have $\delta^{18}\text{O}_w$ values between +4.7 and +10.3‰. These high values are consistent with water
509 isotopically buffered by host rocks during burial history, or with the involvement of highly
510 evaporated water (Bradbury and Woodwell, 1987; Longstaffe, 1987). If fluid flow has
511 occurred, it has not acted long enough or in a volume sufficient to maintain an oxygen
512 isotopic imbalance of oxygen with the host rocks (e.g., Bradbury and Woodwell, 1987).

513 The $\delta^{13}\text{C}$ values of the youngest veins are generally homogeneous, ranging from -0.9
514 to +0.9‰, values compatible with waters of marine origin or having been isotopically
515 buffered by marine carbonate rocks. Only the SE3 vein shows a significant difference with its
516 host rock (+0.1 versus -1.6‰), which is once again in the direction of an incursion of water in
517 isotopic imbalance with the surrounding rock. To summarize, the late veins studied show two
518 distinct paleohydrological regimes, with either evidence of meteoric water circulation or the
519 presence of isotopically buffered waters and therefore possibly of more local origin. The
520 recording of these two sources of fluids in tectonic veins is consistent with other continental
521 fold and thrust belts (e.g., Roure et al., 2005 and references therein; Travé et al., 2007; Cruset
522 et al, 2020). Examples include the Canadian Rockies (Garven, 1985), the Mexican fold and
523 thrust belt (Fitz-Diaz et al., 2011), the Albanides (Vilasi et al., 2009), but also the central and
524 eastern South Pyrenean fold and thrust belt, as shown in the Jaca and Cotiella thrusts (Lacroix
525 et al., 2014; Travé et al., 1997) or the Lower Pedraforca thrust sheet (Cruset et al., 2020). In
526 all these settings, and as we infer in the SPFT, marine-derived or isotopically buffered waters
527 were dominant in volume, but topographic highs acted as recharge areas for meteoric waters,
528 which flowed downward along faults, or in aquifers, to locally replace the initial fluids.

529 Concerning sample SE10 and the 4 undated veins, because of the possibility of
530 clumped isotope reordering, only their $\delta^{13}\text{C}$ values can be tentatively used to decipher the
531 origin of the water that allowed their precipitation. The measured values are generally close to

532 those observed for younger veins, consistent with marine or buffered water. Only SE10 vein
533 has a $\delta^{13}\text{C}$ value significantly lower than that of the host rock (-4.5‰ versus -0.6‰). It
534 indicates an organic origin of part of the carbon that could be soil derived or produced by
535 microbially-mediated redox reactions (Hoefs, 2018).

536 Finally, the $\delta^{18}\text{O}$ of host rocks is too negative compared to those expected for marine
537 sediments, with values below -2.4‰ (Figure 5C). For the Arguis-Pamplona marls, low values
538 could be explained at least in part by the presence of a detrital carbonate fraction with
539 negative signature. For the other formations, corresponding to platform carbonates, they
540 necessarily indicate an alteration of the initial isotopic composition. It could result from burial
541 recrystallization related to temperature increase, or from a partial reset during the ingress of
542 large volumes of water in isotopic disequilibrium with the carbonates (e.g., Bradbury and
543 Woodwell, 1987). A precise determination of the diagenetic evolution of the deposits
544 involved in the SPFT would be necessary to determine the timing and conditions of such
545 peculiar isotopic evolution, as well as to link it with the long-term evolution of calcite-
546 precipitating water within the tectonic frame of the southern Pyrenees.

547

548 **Conclusions**

549 The example of the South Pyrenean Frontal Thrust demonstrates the potential of
550 $\Delta 47/\text{U-Pb}$ thermo-chronometry to determine the conditions of fracture development and
551 associated vein precipitation in tectonically complex areas such as fold and thrust belts. The
552 ages obtained, which range between ~61 Ma and ~14 Ma, are sometimes clearly distinct from
553 the estimates derived from the microstructural study of fractures, highlighting the relevance of
554 absolute dating in fracture analysis. Most studied veins formed during the late exhumation of
555 the area (age < 28 Ma), and the most recent ages obtained likely record the last tectonic pulses
556 of the southern Pyrenees. This late formation makes it possible to validate the vein T $\Delta 47$

557 values, which were not modified by reordering during burial. Calculation of the oxygen
558 isotopic compositions of the waters shows that the veins record either the incursion of
559 meteoric water from the surface, or the presence of waters of more local origin that have
560 interacted with the surrounding rocks. The modelling of the thermal evolution of the SPFT
561 indicates that during maximum burial at around 28 Ma, temperatures could reach 120-140°C
562 at the base of the series. For undated or older veins, clumped isotope reordering models
563 suggest that such temperatures have been sufficient to significantly alter clumped isotopes
564 values, excluding their use as a reliable thermal marker or paleohydrological tracer. Thus, in
565 areas where temperatures higher than 100°C have been reached, the use of clumped on
566 diagenetic calcite veins or cements should systematically be accompanied by the modelling of
567 clumped isotope reordering. In this purpose defining the thermal history of the area under
568 investigation is a mandatory pre-requisite, and determining the precipitation ages with the U-
569 Pb method is a definite advantage.

570

571 **Acknowledgements**

572 This work benefited from a PhD grant of the French Ministry of Research (MESR) to
573 NC. All analyses and field work performed in the course of this study were funded by a
574 “CNRS excellence chair” grant to GH. The manuscript greatly benefited from the reviews of
575 P. Granado and two anonymous reviewers.

576

577 **References**

578 Allen, P., Allen, J., 2013. Basin analysis: principles and application to petroleum play
579 assessment (Third edition). Wiley-Blackwell, 632 p.

580 Anastasio, D.J., 1987. Thrusting, halotectonics, and sedimentation in the External
581 Sierra, southern Pyrenees, Spain. PhD thesis, Johns Hopkins University, Baltimore, MD.

582 Arenas, C., Millán, H., Pardo, G., Pocoví, A., 2001. Ebro Basin continental
583 sedimentation associated with late compressional Pyrenean tectonics (north-eastern Iberia):
584 controls on basin margin fans and fluvial systems. *Basin Res.* 13, 65–89. <https://doi.org/10.1046/j.1365-2117.2001.00141.x>.
585

586 Babault, J., Van Den Driessche, J., Bonnet, S., Castelltort, S., Crave, A., 2005. Origin of
587 the highly elevated Pyrenean peneplain. *Tectonics*, 24, TC2010. doi:10.1029/2004TC001697.

588 Beaudoin, N., Lacombe, O., Roberts, N. M.W., Koehn, D., 2018. U-Pb dating of calcite
589 veins reveals complex stress evolution and thrust sequence in the Bighorn Basin, Wyoming,
590 USA. *Geology*, 46 (11), 1015-1018.

591 Beaudoin, N., Huyghe, D., Bellahsen, N., Lacombe, O., Emmanuel, L., Mouthereau, F.,
592 Ouanhnon, L., 2015. Fluid Systems and Fracture Development During Syn-Depositional Fold
593 Growth: An Example from the Pico Del Aguila Anticline, Sierras Exteriores, Southern
594 Pyrenees, Spain. *J. Struct. Geol.*, 70, 23-38.

595 Beaumont, C., Muñoz, J.A., Hamilton, J., Fullsack, P., 2000. Factors Controlling the
596 Alpine Evolution of the Central Pyrenees Inferred from a Comparison of Observations and
597 Geodynamical Models. *J. Geophys. Res.: Solid Earth*, 105, 8121-8145.

598 Bergbauer, S., Pollard, D.D., 2004. A new conceptual fold-fracture model including
599 prefolding joints, based on the Emigrant Gap anticline, Wyoming. *GSA Bull.*, 116 (3-4), 294–
600 307. doi: <https://doi.org/10.1130/B25225.1>

601 Bergman, S.C., Huntington, K.W., Crider, J.G., 2013. Tracing Paleofluid Sources Using
602 Clumped Isotope Thermometry of Diagenetic Cements Along the Moab Fault, Utah. *Am. J.*
603 *Sci.*, 313, 490-515.

604 Bonifacie M., Calmels D., Eiler J.M., Horita, J., Chaduteau C., Vasconcelos, C.,
605 Agrinier, P., Katz A., Passey, B.H., Ferry J.M., Bourrand J.J., 2017. Experimental calibration
606 of the dolomite clumped isotope thermometer from 25 to 350°C, and implications for a

607 universal calibration for all (Ca, Mg, Fe)CO₃ carbonates. *Geochem. Cosmochem. Acta*, 200,
608 255-279, doi: 10.1016/j.gca.2016.11.028

609 Bons, P.D., Elburg, M.A., Gomez-Rivas, E., 2012. A Review of the Formation of
610 Tectonic Veins and Their Microstructures. *J. Struct. Geol.*, 43, 33-62.

611 Bradbury, H.J., Woodwell, G.R., 1987. Ancient fluid flow within foreland terrains. In:
612 Goff, J.C., Williams, B.P.J. (Eds.), *Fluid Flow in Sedimentary Basins and Aquifers*.
613 Geological Society, London, Special Publications 34, 87–102.

614 Cantarelli, V., 2011. Tectonic-sedimentation Burial History and Exhumation of the
615 Southern Sector of the Central-western Pyrenees. PhD Thesis, University of Camerino, Spain.

616 Carbayo, A., León, L., Puigdefàbregas, C., 1972, Mapa Geológico De España a Escala
617 1:50000. Hoja 117 (Ochagavía). IGME, Spain.

618 Carr, A., 2000. Suppression and Retardation of Vitrinite Reflectance, Part 1. Formation
619 and Significance for Hydrocarbon Generation. *J. Petr. Geol.*, 23, 313-343.

620 Choukroune, P., Roure, F., Pinet, B. & Team, E.P., 1990. Main Results of the Ecos
621 Pyrenees Profile. *Tectonophysics*, 173, 411-423.

622 Coney, P. J., Muñoz, J.A., McClay, K.R., Evenchick, C.A., 1996. Syntectonic burial
623 and post-tectonic exhumation of the southern Pyrenees foreland fold-thrust belt. *J. Geol. Soc.*,
624 London, 153, 9-16.

625 Crognier, N., Hoareau, G., Aubourg, C., Dubois, M., Lacroix, B., Branellec, M., Callot,
626 J. P., Vennemann, T., 2018. Syn-orogenic fluid flow in the Jaca basin (south Pyrenean fold
627 and thrust belt) from fracture and vein analyses. *Bas. Res*, 30, 187-216.
628 doi:10.1111/bre.12249

629 Cruset, D., Cantarero, I., Benedicto, A., John, C.M., Vergés, J., Albert, R., Gerdes, A.,
630 Travé, A., 2020. From hydroplastic to brittle deformation: Controls on fluid flow in fold and

631 thrust belts. Insights from the Lower Pedraforca thrust sheet (SE Pyrenees). *Mar. Petr. Geol.*,
632 120, 104517, doi: <https://doi.org/10.1016/j.marpetgeo.2020.104517>.

633 De Rojas, B.J., Latorre, F., 1972. Mapa Geológico De España a Escala 1:50000. Hoja
634 175 (Sigüés). IGME, Spain.

635 Dennis, K.J., Affek, H.P., Passey, B.H., Schrag, D.P., Eiler, J.M., 2011. Defining an
636 Absolute Reference Frame for 'Clumped' isotope Studies of CO₂. *Geochem. Cosmochim.*
637 *Acta*, 75, 7117-7131.

638 Dromgoole, E.L., Walter, L.M., 1990. Iron and Manganese Incorporation into Calcite:
639 Effects of Growth Kinetics, Temperature and Solution Chemistry. *Chem. Geol.*, 81, 311-336.

640 Engelder, T., 1985. Loading paths to joint propagation during a tectonic cycle: an
641 example from the Appalachian Plateau, *J. Struct. Geol.*, 7, 459-476.

642 Filleaudeau, P.-Y., 2011. Croissance et dénudation des Pyrénées du Crétacé Supérieur
643 au Paléogène : apports de l'analyse de bassin et thermochronométrie détritique. PhD thesis,
644 Université Pierre et Marie Curie - Paris 6, Paris, France, 370 p.

645 Fitz-Diaz, E., Hudleston, P., Siebenaller, L., Kirschner, D., Camprubí, A., Tolson, G.,
646 Puig, T.P., 2011. Insights into fluid flow and water-rock interaction during deformation of
647 carbonate sequences in the Mexican fold-thrust belt. *J. Struct. Geol.*, 33, 1237-1253.

648 Garcia-Sansegundo, J., Montes, M.J., Garrido, E.A., Barnolas, A., A., B., 1992. Mapa
649 Geológico De España a Escala 1:50000. Hoja 209 (Agüero). IGME, Spain.

650 Garven, G., 1985. The Role of Regional Fluid Flow in the Genesis of the Pine Point
651 Deposit, Western Canada Sedimentary Basin. *Econ. Geol.*, 80, 307-324.

652 Ghosh, P., Adkins, J., Affek, H., Balta, B., Guo, W., Schauble, E.A., Schrag, D., Eiler,
653 J.M., 2006. 13 C–18 O Bonds in Carbonate Minerals: A New Kind of Paleothermometer.
654 *Geochem. Cosmochim. Acta*, 70, 1439-1456.

655 Goldstein, R.H., Reynolds, T.J., 1994. Systematics of Fluid Inclusions in Diagenetic
656 Minerals. Sepm Short Course 31, Society for Sedimentary Geology, 199 p.

657 Guo, W., Mosenfelder, J.L., Goddard, W.A., Eiler, J.M., 2009. Isotopic Fractionations
658 Associated with Phosphoric Acid Digestion of Carbonate Minerals: Insights from First-
659 Principles Theoretical Modeling and Clumped Isotope Measurements. *Geochem. Cosmochim.*
660 *Acta Acta*, 73, 7203-7225.

661 Hoefs, J., 2018. Stable isotope geochemistry. Springer Textbooks in Earth Sciences,
662 Geography and Environment, Springer, 437 p.

663 Hodson, K.R., Crider, J.G., Huntington, K.W., 2016. Temperature and Composition of
664 Carbonate Cements Record Early Structural Control on Cementation in a Nascent
665 Deformation Band Fault Zone: Moab Fault, Utah, USA. *Tectonophysics*, 690, 240-252,
666 doi:10.1016/j.tecto.2016.04.032

667 Horstwood, MSA, Košler, J, Gehrels, G, Jackson, SE, Mclean, NM, Paton, C, Pearson,
668 NJ, Sircombe, K, Sylvester, P, Vermeesch, P, Bowring, JF, Condon, DJ, Schoene, B., 2016.
669 Community-Derived Standards for LA-ICP-MS U-(Th-)Pb Geochronology - Uncertainty
670 Propagation, Age Interpretation and Data Reporting. *Geostand. Geoanal. Res.* 40(3), 311-332,
671 doi :10.1111/j.1751-908X.2016.00379.x.

672 Huntington, K., Eiler, J., Affek, H., Guo, W., Bonifacie, M., Yeung, L., Thiagarajan, N.,
673 Passey, B., Tripathi, A., Daëron, M., 2009. Methods and Limitations of ‘Clumped’ CO₂
674 Isotope ($\Delta 47$) Analysis by Gas-Source Isotope Ratio Mass Spectrometry. *J. Mass Spectrom.*,
675 44, 1318-1329.

676 Huyghe, D., Mouthereau, F., Castelltort, S., Filleaudeau, P.Y., Emmanuel, L., 2009.
677 Paleogene Propagation of the Southern Pyrenean Thrust Wedge Revealed by Finite Strain
678 Analysis in Frontal Thrust Sheets: Implications for Mountain Building. *Earth Planet. Sci.*
679 *Lett.*, 288, 421-433.

680 Izquierdo-Llavall, E., Aldega, L., Cantarelli, V., Corrado, S., Gil-Peña, I., Invernizzi,
681 C., Casas, A.M., 2013. On the Origin of Cleavage in the Central Pyrenees: Structural and
682 Paleo-Thermal Study. *Tectonophysics*, 608, 303-318.

683 Kim, S.-T., O'Neil, J. R., 1997. Equilibrium and nonequilibrium oxygen isotope effects
684 in synthetic carbonates *Geochim. Cosmochim. Ac.*, 61, 3461–3475, 1997.

685 Labaume, P., Meresse, F., Jolivet, M., Teixell, A., Lahfid, A., 2016. Tectonothermal
686 history of an exhumed thrust-sheet-top basin: An example from the south Pyrenean thrust
687 belt. *Tectonics*, 35, doi:10.1002/ 2016TC004192.

688 Labaume, P., Teixell, 2018. 3D structure of subsurface thrusts in the eastern Jaca Basin,
689 southern Pyrenees. *Geol. Acta*, 16-4, 477-498

690 Lacroix, B., Travé, A., Buatier, M., Labaume, P., Vennemann, T., Dubois, M., 2014.
691 Syntectonic fluid-flow along thrust faults: Example of the South-Pyrenean fold-and-thrust
692 belt. *Mar. Petr. Geol.*, 49, 84-98.

693 Lacroix, B., Baumgartner, L., Bouvier, A.S., Kempton, P., Vennemann, T. 2018. Multi
694 Fluid-Flow Record during Episodic Mode I Opening: A Microstructural and SIMS Study
695 (Cotiella Thrust Fault, Pyrenees). *Earth Planet. Sci. Lett.* DOI 10.1016/j.epsl.2018.09.016

696 Lafargue E., Marquis, F., Pillot, D., 1998. Rock-Eval 6 applications in hydrocarbon
697 exploration, production, and soil contamination studies: *Rev. Inst. Fr. Pétr.*, 53, 4, 421–437.

698 Lawson M, Shenton BJ, Stolper DA, Eiler JM, Rasbury ET, Becker TP, Phillips-Lander
699 C, Buono AS, Becker SP, Pottorf R, Gray GG, Yurewicz D, Gournay J, 2017. Deciphering
700 the diagenetic history of the El Abra Formation of eastern Mexico using reordered clumped
701 isotope temperatures and U-Pb dating. *GSA Bull.*, 130(3–4), 617–629

702 Lloyd, M.K, Ryb, U., Eiler, J.M., 2018. Experimental calibration of clumped isotope
703 reordering in dolomite. *Geochim. Cosmochim. Acta*, 242, 1–20

704 Longstaffe, F., 1987. Stable Isotope Studies of Diagenetic Processes. In: Short Course
705 in Stable Isotope Geochemistry of Low Temperature Fluids (Ed. by T. K. Kyser), 13, 187-
706 257. Mineralogical Association of Canada, Toronto.

707 Luetkemeyer, P.B., Kirschner, D.L., Huntington, K.W., Chester, J.S., Chester, F.M.,
708 Evans, J.P., 2016. Constraints on paleofluid sources using the clumped-isotope thermometry
709 of carbonate veins from the SAFOD (San Andreas Fault Observatory at Depth) borehole.
710 *Tectonophysics*, 690, 174–189.

711 MacDonald, J.M., Faithfull, J.W., Roberts, N.M.W., Davies, A.J.; Holdsworth,
712 C.M., Newton, M., Williamson, S., Boyce, A., John, C.M. 2019. Clumped-isotope
713 palaeothermometry and LA-ICP-MS. U–Pb dating of lava-pile hydrothermal calcite veins.
714 *Contrib. Mineral. Petrol.*, 174, 63. <https://doi.org/10.1007/s00410-019-1599-x>

715 Machel H.G., 2000. Application of Cathodoluminescence to Carbonate Diagenesis. In:
716 Pagel M., Barbin V., Blanc P., Ohnenstetter D. (eds) *Cathodoluminescence in Geosciences*.
717 Springer, Berlin, Heidelberg

718 Mangenot X., Gerdes A., Gasparrini M., Bonifacie M., Rouchon V., 2018. An emerging
719 thermo-chronometer for carbonate-bearing rocks: $\Delta 47/(U-Pb)$. *Geology*, 46(12), 1067-1070

720 Millán Garrido, H., Aurell, M., Meléndez, A. (1994) Synchronous Detachment Folds
721 and Coeval Sedimentation in the Prepyrenean External Sierras (Spain): A Case Study for a
722 Tectonic Origin of Sequences and Systems Tracts. *Sedimentology*, 41, 1001-1024.

723 Millán Garrido, H., Pueyo-Morer, E., Aurell-Cardona, M., Luzón-Aguado, A., Oliva-
724 Urcia, B., Martínez-Peña, B., 2000. Actividad tectónica registrada en los depósitos terciarios
725 del frente meridional del Pirineo central. Translated title: Tectonic activity recorded in the
726 tertiary deposits of the southern front of the central Pyrenees. *Rev. Soc. Geol. Esp.*, 13 (2),
727 279-300.

728 Mochales, T., Casas, A.M., Pueyo, E.L., Barnolas, A., 2012. Rotational velocity for
729 oblique structures (Boltaña anticline, Southern Pyrenees): *J. Struct. Geol.*, 35, 2-16.

730 Montes, M.J., Barnolas, A., 1992. Mapa Geológico De España a Escala 1:50000. Hoja
731 210 (Yebra De Basa). IGME, Spain.

732 Montes, M.J., Barnolas, A., 2002. Estratigrafía Del Eoceno - Oligoceno De La Cuenca
733 De Jaca (Sinclinatorio Del Guarga). PhD Tesis, Universidad de Barcelona, 365 p.

734 Muñoz J.A., 1992. Evolution of a continental collision belt: ECORS-Pyrenees crustal
735 balanced cross-section. In: McClay K.R. (Eds.), *Thrust Tectonics*. Springer, Dordrecht, pp.
736 235–246.

737 Muñoz, J.A., 2002. Alpine tectonics I: the Alpine system north of the Betic Cordillera.
738 Tectonic setting; The Pyrenees. In: W. Gibbons, T. Moreno (Eds.), *Geology of Spain*, Geol.
739 Soc (London), pp. 370-385.

740 Muñoz, J.-A., Beamud, E., Fernández, O., Arbués, P., Dinarès-Turell, J., Poblet, J.
741 2013. The Ainsa Fold and thrust oblique zone of the central Pyrenees: Kinematics of a curved
742 contractional system from paleomagnetic and structural data, *Tectonics*, 32, 1142- 1175,
743 doi:10.1002/tect.20070.

744 Muñoz, J.A., Mencos, J., Roca, E., Carrera, N., Gratacós, O., Ferrer, O., Fernández, O.,
745 2018. The structure of the South-Central-Pyrenean fold and thrust belt as constrained by
746 subsurface data. *Geol. Acta*, 16 (4), 439-460.

747 Ogg, J.G., Ogg, G.M., Gradstein, F.M., 2016. *A Concise Geological Time Scale*.
748 Elsevier, 229 p.

749 Oliva-Urcia, B., Pueyo, E. L., 2007. Rotational basement kinematics deduced from
750 remagnetized cover rocks (Internal Sierras, southwestern Pyrenees), *Tectonics*, 26, TC4014,
751 doi:10.1029/2006TC001955.

752 Oliva-Urcia, B., Beamud, E., Garcés, M., Arenas, C., Soto, R., Pueyo, E.L., Pardo, G.,
753 2016. New magnetostratigraphic dating of the Palaeogene syntectonic sediments of the west-
754 central Pyrenees: tectonostratigraphic implications. In: Pueyo, E.L., Cifelli, F., Sussman, A.J.,
755 Oliva-Urcia, B. (Eds.), *Palaeomagnetism in Fold and Thrust Belts: New Perspectives*.
756 Geological Society, London, Special Publications, vol. 425. pp. 107–128.
757 <https://doi.org/10.1144/SP425.5>.

758 Oliva-Urcia, B., E. Beamud, C. Arenas, E.L. Pueyo, M. Garcés, R. Soto, L. Valero, F.J.
759 Pérez-Rivarés, 2019. Dating the northern deposits of the Ebro foreland basin; implications for
760 the kinematics of the SW Pyrenean front, *Tectonophysics*, Volume 765, 2019, 11-34,
761 <https://doi.org/10.1016/j.tecto.2019.05.007>.

762 Price L.C., Barker, C.E., 1985. Suppression of vitrinite reflectance in amorphous rich
763 kerogen - A major unrecognized problem: *J. Petr. Geol.*, 8, 59-84

764 Pueyo, E., Millán, H., Pocovi, A., 2002. Rotation Velocity of a Thrust: A Paleomagnetic
765 Study in the External Sierras (Southern Pyrenees). *Sed. Geol.*, 146, 191-208.

766 Roberts, N.M., Walker, R.J., 2016. U-Pb Geochronology of Calcite-Mineralized Faults:
767 Absolute Timing of Rift-Related Fault Events on the Northeast Atlantic Margin. *Geology*,
768 G37868. 37861.

769 Roberts, N.M.W., Rasbury, E.T., Parrish, R.R., Smith, C.J., Horstwood, M.S.A.,
770 Condon, D.J., 2017. WC-1: A calcite reference material for LA-ICP-MS U-Pb
771 geochronology, *Geochem., Geophys., Geosyst.*, 18, 2807-2814, doi: 10.1002/2016GC006784.

772 Roure, F., Swennen, R., Schneider, F., Faure, J., Ferket, H., Guilhaumou, N., Osadetz,
773 K., Robion, P., Vandeginste, V., 2005. Incidence and Importance of Tectonics and Natural
774 Fluid Migration on Reservoir Evolution in Foreland Fold-and-Thrust Belts. *Oil & gas sci.*
775 *technol.*, 60, 67-106.

776 Samsó, J.M., Sanz, J., García, J., Serra, J., Tosquella, J., Garrido, E.A., Barnolas, A.,
777 1991. Mapa Geológico De España a Escala 1:50000. Hoja 248 (Apiés). IGME, Spain.

778 Soler-Sampere, M., Puigdefàbregas, C., 1970. Líneas Generales De La Geología Del
779 Alto Aragón Occidental. Pirineos, 96, 5-20

780 Stolper, D.A., Eiler, J.M., 2015. The Kinetics of Solid-State Isotope-Exchange
781 Reactions for Clumped Isotopes: A Study of Inorganic Calcites and Apatites from Natural and
782 Experimental Samples. *Am. J. Sci.*, 315, 363-411.

783 Tavani, S., Storti, F., Lacombe, O., Corradetti, A., Muñoz, J. Mazzoli, S., 2015. A
784 review of deformation pattern templates in foreland basin systems and fold-and-thrust belts:
785 implications for the state of stress in the frontal regions of thrust wedges. *Earth Sci. Rev.*, 141,
786 82–104.

787 Teixell, A., Montes, M.J., Arenas, C., Garrido, E.A., 1992. Mapa Geológico De España
788 a Escala 1:50000. Hoja 208 (Uncastillo). IGME, Spain.

789 Teixell, A., 1996. The Ansó transect of the southern Pyrenees: basement and cover
790 thrust geometries. *Journal of the Geological Society*, 153(2), 301-
791 310. <https://doi.org/10.1144/gsjgs.153.2.0301>

792 Teixell, A., Labaume, P., Ayarza, P., Espurt, N., de Saint Blanquat, M., Lagabrielle, Y.,
793 2018. Crustal structure and evolution of the Pyrenean-Cantabrian belt: A review and new
794 interpretations from recent concepts and data. *Tectonophysics*, 724-725, 146-
795 170. <https://doi.org/10.1016/j.tecto.2018.01.009>

796 Travé A., Labaume P., Vergés J., 2007. Fluid Systems in Foreland Fold-and-Thrust
797 Belts: An Overview from the Southern Pyrenees. In: Lacombe O., Roure F., Lavé J., Vergés
798 J. (Eds), *Thrust Belts and Foreland Basins*. *Frontiers in Earth Sciences*. Springer, Berlin,
799 Heidelberg, pp. 93-115. https://doi.org/10.1007/978-3-540-69426-7_5

800 Travé, A., Labaume, P., Calvet, F., Soler, A., 1997. Sediment Dewatering and Pore
801 Fluid Migration Along Thrust Faults in a Foreland Basin Inferred from Isotopic and
802 Elemental Geochemical Analyses (Eocene Southern Pyrenees, Spain). *Tectonophysics*, 282,
803 375-398.

804 Turner, J., 1988. Tectonic and Stratigraphic Evolution of the West Jaca Thrust-Top
805 Basin, Southwest Pyrenees, PhD thesis, University of Bristol.

806 Twiss, R.J., Moores, E.M., 2006. *Structural Geology*, 2nd edition, Freeman & Co, 532
807 p.

808 Vilasi, N., Malandain, J., Barrier, L., Callot, J.P., Guilhaumou, N., Lacombe, O.,
809 Muska, K., Roure, F., Swennen, R. (2009). From outcrop and petrographic studies to basin-
810 scale fluid flow modelling: the use of the Albanian natural laboratory for carbonate reservoir
811 characterization, *Tectonophysics*, 474, 367-392.

812 Zachos, J., Pagani, M., Sloan, L., Thomas, E., Billups, K., 2001. Trends, Rhythms, and
813 Aberrations in Global Climate 65 Ma to Present. *Science*, 292, 686-693.

814

815 TABLES

816

817 **Table S1:** Results of isotopic, microthermometric and U-Pb dating measurements for the
818 studied veins and their host-rocks.

819

820 **Table S2:** calcite U-Pb analyses for standards (WC1, Duff Brown) and successful samples
821 (SE3, SE4, SE10, A21, A22, A56)

822

823 **Table S3:** Results of Rock-Eval Tmax analyses

824

Figure captions

825

826

827 **Figure 1.** A: Simplified geological map of the Pyrenees (modified from Filleaudeau, 2011).
828 The black line locates the cross-section in B, and the red frame the studied area in C. B:
829 Balanced cross section of the Jaca Basin including the Sierras Exteriores to the south
830 (modified from Labaume et al., 2016 and Labaume and Teixell, 2018). C: Geological map of
831 the Sierras Exteriores based on Garcia-Sanseguno et al. (1992), Samsó et al. (1991) and
832 Teixell et al. (1992), with location of the studied sites and samples. D, E: closer views of the
833 two main areas investigated. Symbols refer to the type of analysis made on the samples (see
834 key). Virtual sedimentary logs: 1: San Felices; 1-2: Riglos and top San Felices; 3: Nueno; 3-4:
835 Pico Del Aguila and top Nueno.

836

837 **Figure 2:** Results of fracture analysis in 7 of the 10 studied sites. Results are presented on 3
838 diagrams (Schmidt' lower-hemisphere, equal-area stereonets) displaying raw data in current
839 bedding attitude (left), corrected for fold axial plunge related to the Guarga thrust activation
840 (middle) and corrected for local bedding dip (right). See text for details. For site A22, where
841 the sampled vein corresponds to a right-lateral fault, the stereogram represents the results of
842 fault-slip inversion calculations, and is directly taken from Beaudoin et al. (2015). Computed
843 stress axes are reported as stars with three branches (σ_1), four branches (σ_2) and five branches
844 (σ_3). Convergent black arrows indicate the direction of compression.

845

846 **Figure 3:** A. Close field view of vein SE3 (arrows). B. Field photograph of vein SE10
847 (arrows, highlighted in black). The fracture network as well as two faults (green arrows) are
848 visible. Red dots refer to the orientation of bedding. C. Field view of site SE4. Arrows point
849 to fractures belonging the dominant fracture set. Red dots refer to the orientation of bedding.

850 D. Field view of site SE12, characterized by a complex fracture network. Red dots refer to the
851 orientation of bedding. E. Mosaics of optical (PPL) and CL photomicrographs across vein
852 SE1. Green arrow points to a stretched crystal typical of syn-opening growth. White arrow
853 points to void-filling calcite with brighter orange CL (see text). Scale bar = 1 mm. F. Optical
854 (PPL) and CL photomicrographs of vein A56, with a blocky texture. Scale bar = 1 mm.

855

856 **Figure 4:** A to E: Mosaics of optical and CL photomicrographs across calcite veins. Scale
857 bars = 1 mm. A. Vein SE4. Stylolites affecting blocky calcites are visible (white arrows). B:
858 Vein A22. In XPL, an increase of grain size is observed towards the center of the vein (left to
859 right). The arrow points to a limit interpreted as reflecting a stage of vein opening. In CL, the
860 color slightly differs on each side of this discontinuity. White line defines the vein border. C.
861 Vein SE2. Numerous shear-related calcite sheets (parallel to the vein wall, here vertical) can
862 be identified. D. Vein SE10. Several generations of blocky calcite can be identified both in
863 PPL and CL. Minor brecciation is also visible to the right of the images. E. Vein SE3.
864 Concentric zoning can be seen on the blocky calcite grains in CL. It follows the trails of
865 primary fluid inclusions visible in XPL (arrows).

866

867 **Figure 5** A. Histogram of homogenization temperatures measured in primary fluids
868 inclusions. Note that for SE10, most fluid inclusions are all liquid. B: Comparison of
869 temperatures obtained with clumped isotopes (using the calibration of Bonifacie et al. (2017)
870 (stars) and with fluid inclusions (bars). Colors of the stars correspond to the age of host-rocks
871 (see legend). C: $\delta^{18}\text{O}$ versus $\delta^{13}\text{C}$ plot of veins and related host-rocks. The numbers refer to
872 sample labels (ex: 56 for A56, 3 for S3, etc). D: Isotopic composition of water calculated
873 from oxygen isotope data of veins and associated clumped isotope temperatures, using the
874 equation of Kim and O'Neil (1997) (all replicates are shown).

875

876 **Figure 6:** Tera-Wasserburg diagrams for the 6 veins successfully dated by the U-Pb method.

877 Red ellipses were not considered in the age calculation. All ellipses correspond to 2 sigma

878 uncertainties.

879

880 **Figure 7:** Results of 1D thermal modelling for the four virtual time-correlated sedimentary

881 logs compiled from previously published logs (see references in the data repository, and

882 location of samples and sections in Figure 1). Stars refer to the age of rocks hosting the veins

883 analyzed for clumped isotopes. For each log, the red dotted frame (upper part of the

884 Campodarbe Fm) corresponds to the thickness of currently eroded sediments that has been

885 added to the model to fit the maturity data (see text for details). Chronostratigraphic

886 correlations from Samsó et al. (1991), García-Sansegundo et al. (1992), Teixell et al. (1992),

887 Montes and Barnolas (2002) and Oliva-Urcia et al. (2016). Tectonic stages from Labaume et

888 al. (2016). Magnetostratigraphic scale from Ogg et al. (2016).

889

890 **Figure 8:** Time-temperature paths for the rocks hosting the 10 veins analyzed for clumped

891 isotopes, as deduced from 1D thermal modelling. The U-Pb ages of dated veins, as well as the

892 range of possible vein precipitation ages calculated from $T\Delta 47$ and assuming thermal

893 equilibrium with the host rocks are indicated. Two exhumation paths are represented (orange

894 and red curves; see text for detail).

895

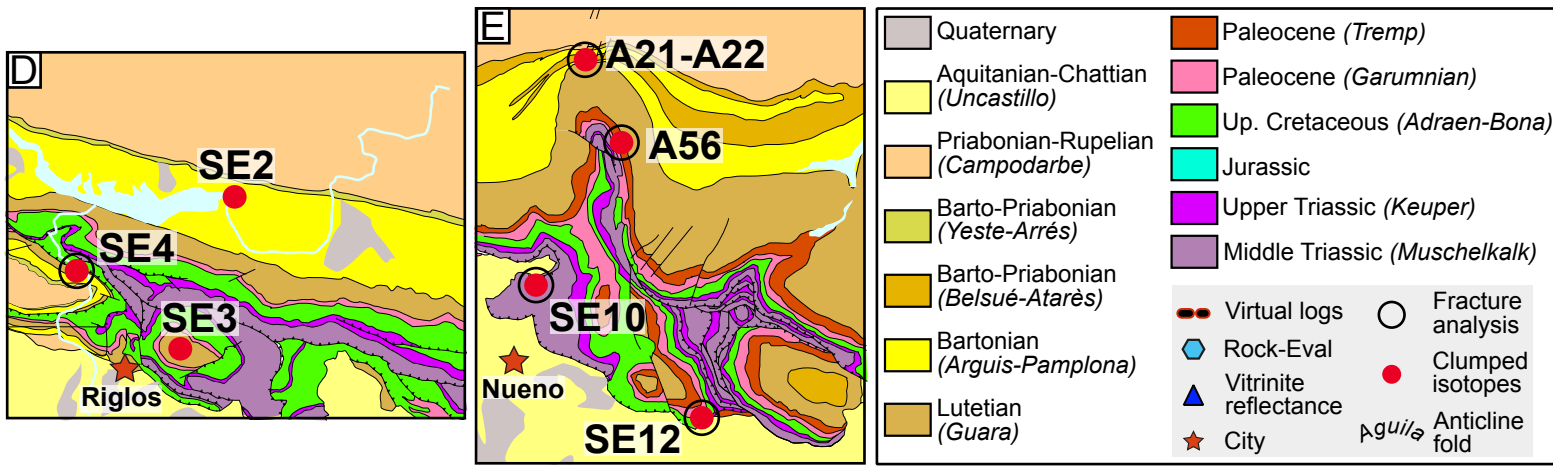
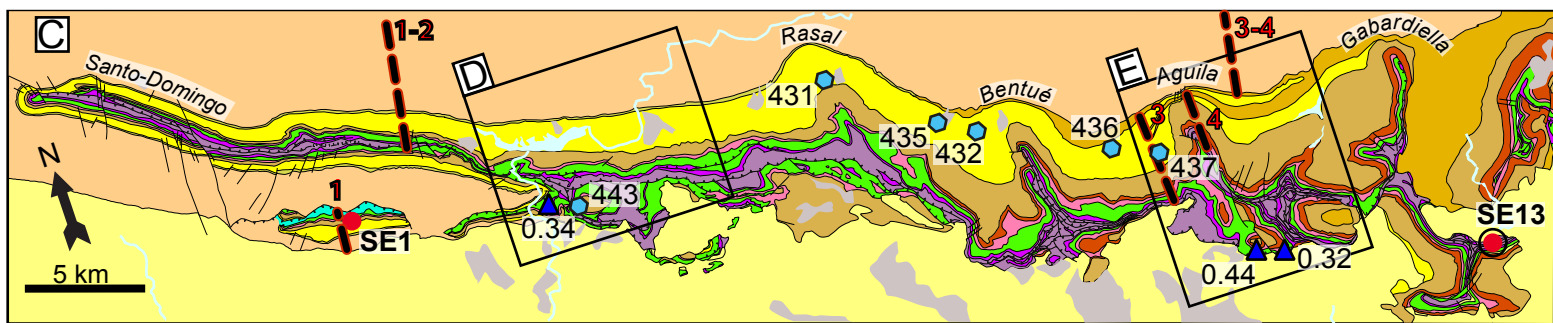
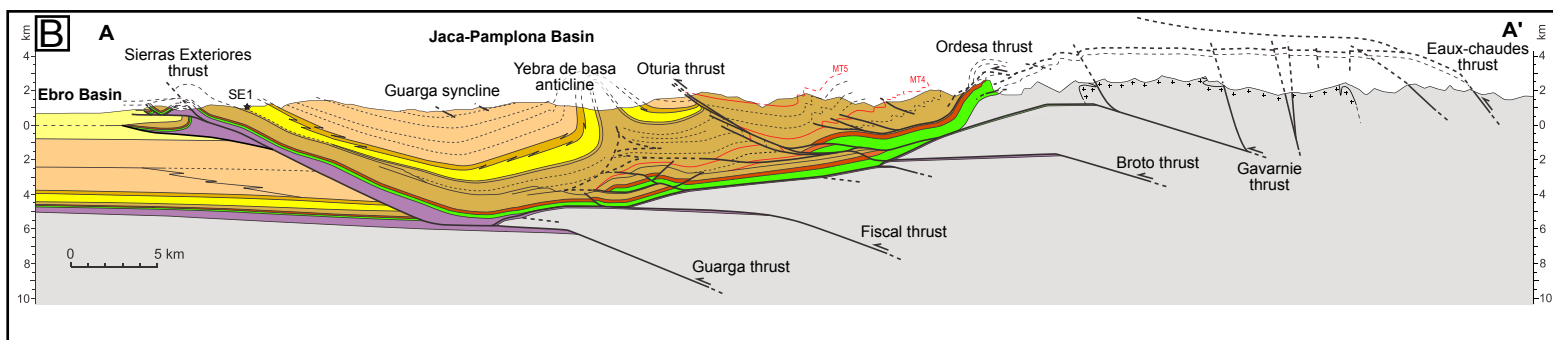
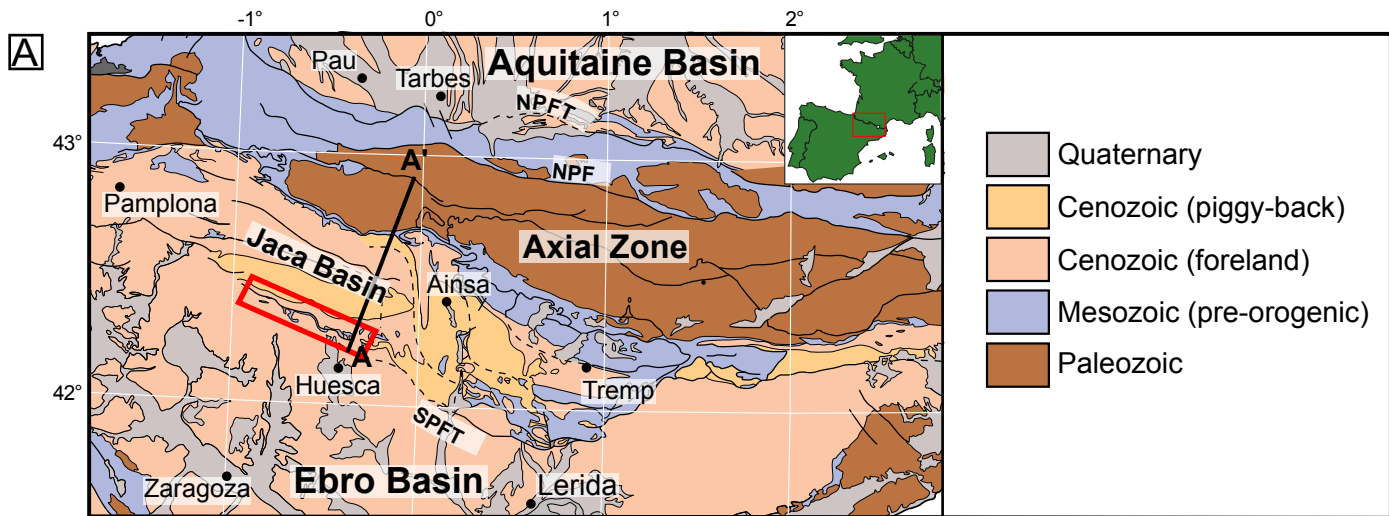
896 **Figure 9:** A. Modelling of the reordering behavior of calcite $T\Delta 47$ (THRM) using the

897 exchange-diffusion model of Stolper and Eiler (2015) and 1D thermal models of the study

898 area. Shaded areas correspond to 2s uncertainties. The measured range of $T\Delta 47$ is indicated

899 between the grey dashed lines. A: Evolution of $T\Delta 47$ for SE10 vein, using 3 distinct starting

900 precipitation temperatures at 60 Ma (20, 43 and 80°C). In the three scenarios, the modelled
901 present-day T Δ 47 is similar to the measured values within uncertainties. B, C: Evolution of
902 T Δ 47 for SE2 vein for several precipitation ages (ranging from 36 to 20 Ma), and
903 precipitation temperatures similar to the enclosing rock. The results for burial and exhumation
904 paths have been represented on two distinct graphs for clarity (B and C, respectively). See
905 text for explanations.
906

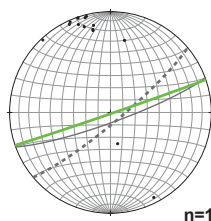
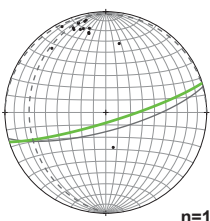
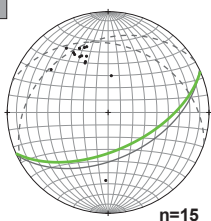


Current attitude of the strata

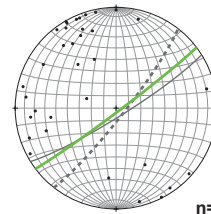
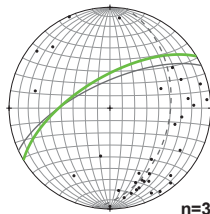
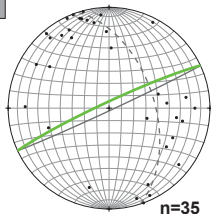
Corrected from thrust activation

Corrected from residual strata tilting

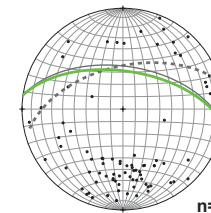
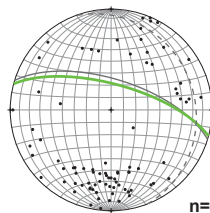
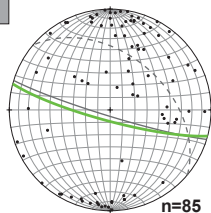
A21



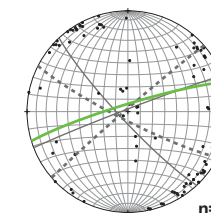
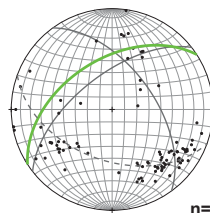
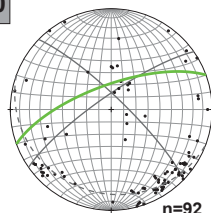
A56



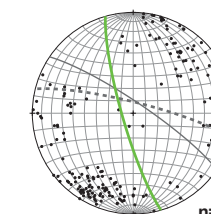
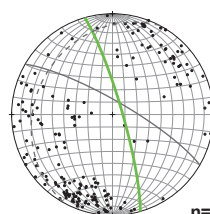
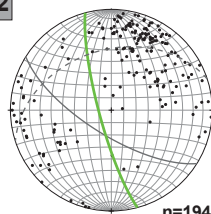
SE4



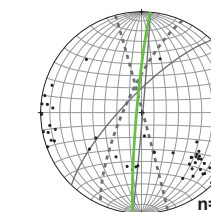
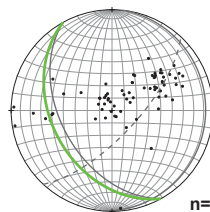
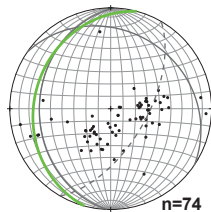
SE10



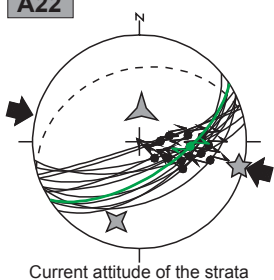
SE12



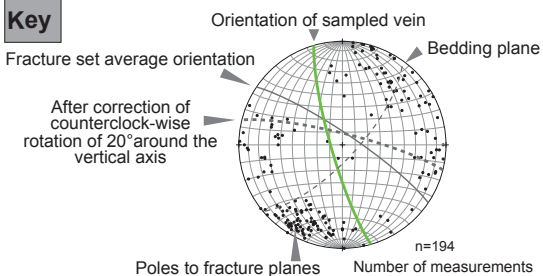
SE13

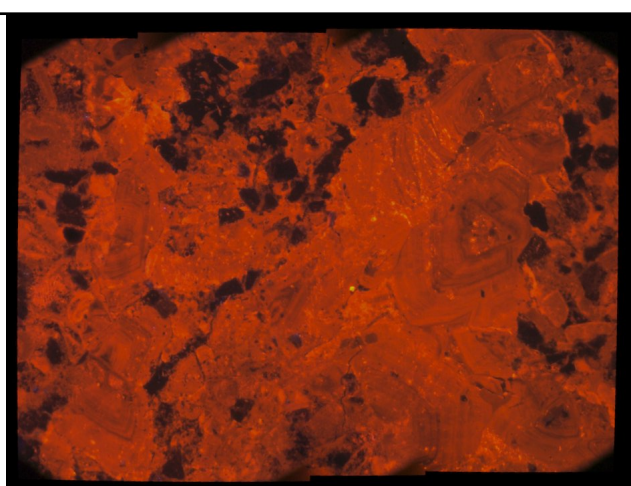
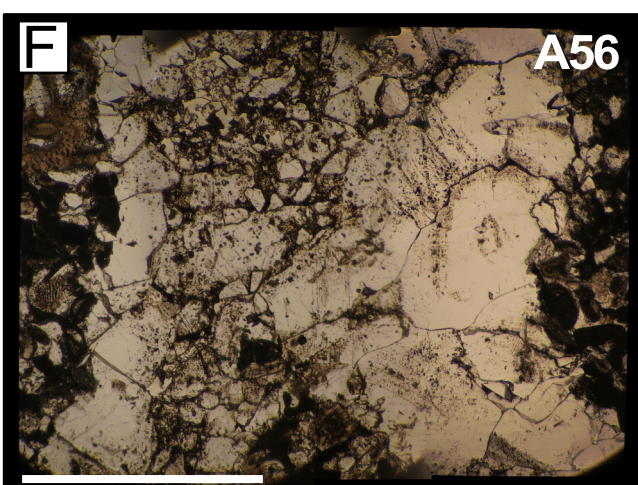
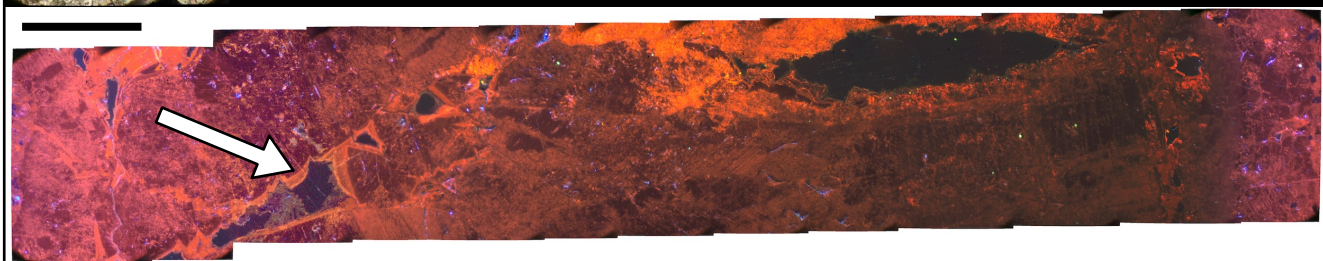
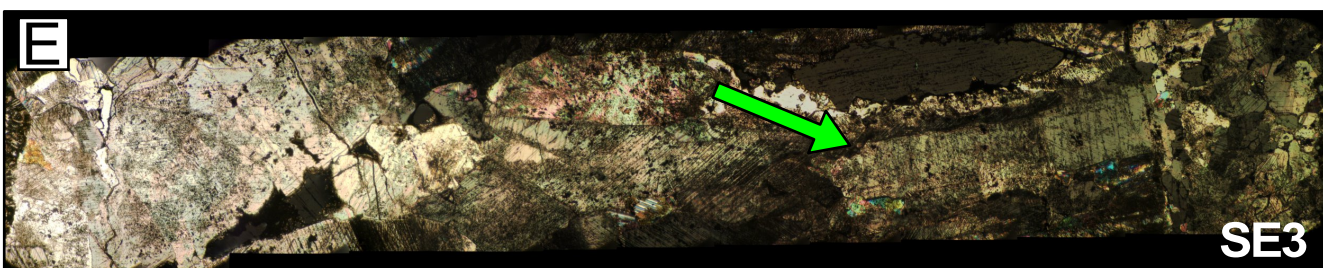
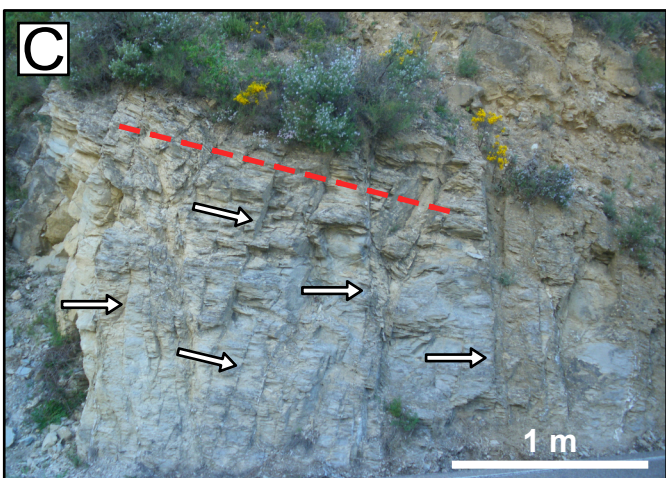
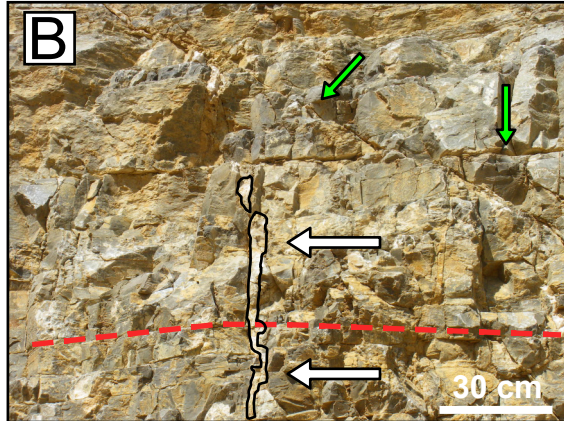


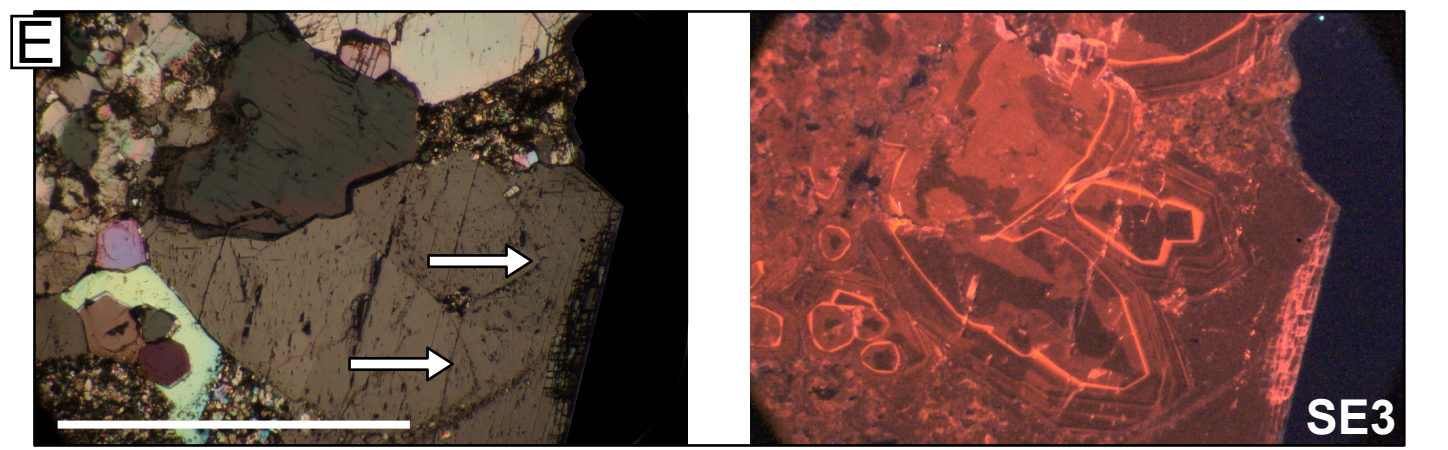
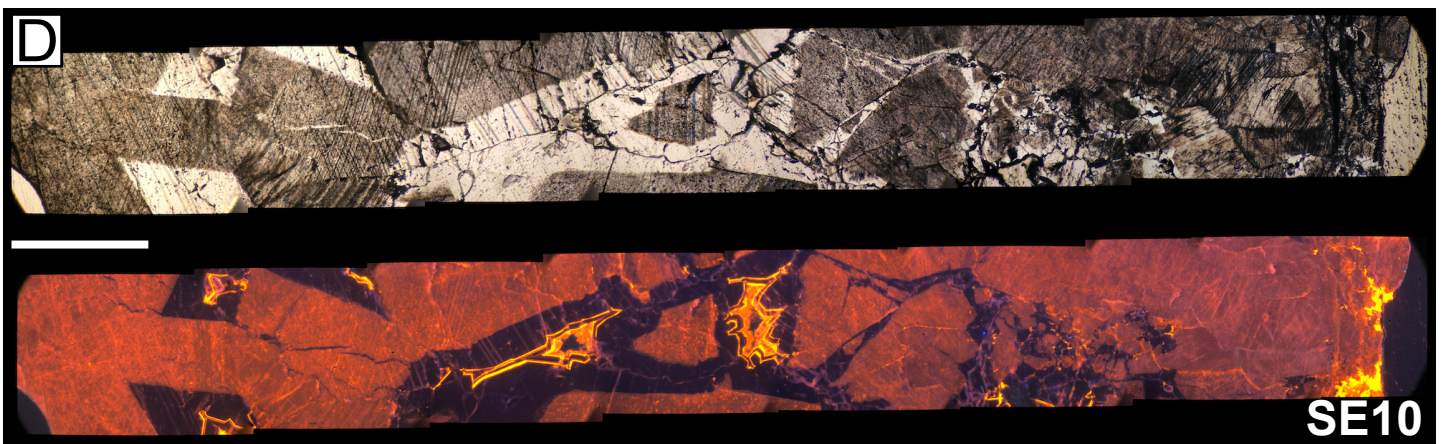
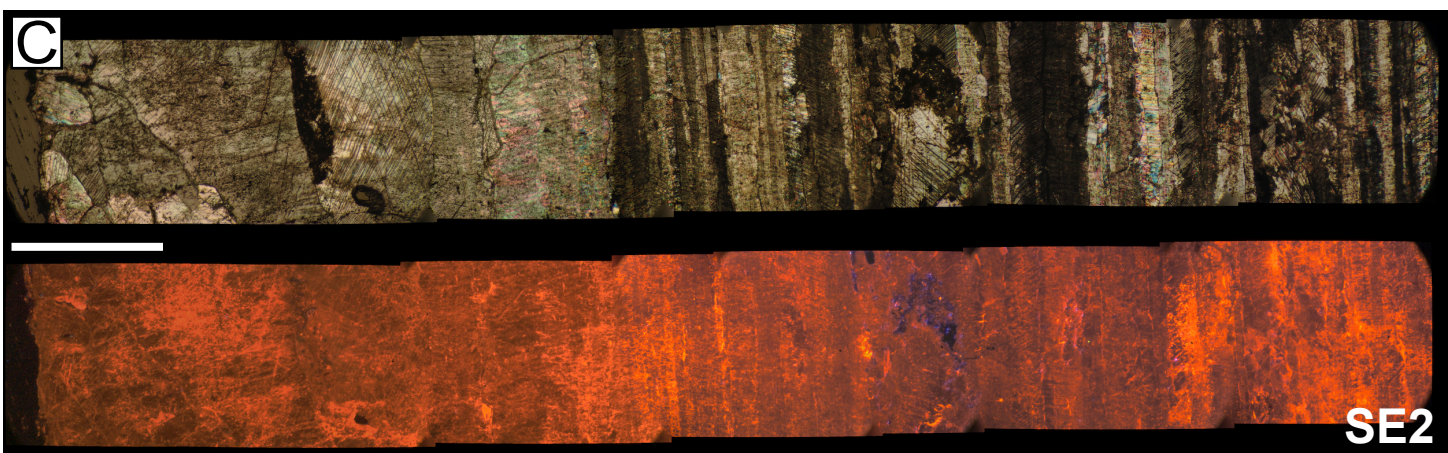
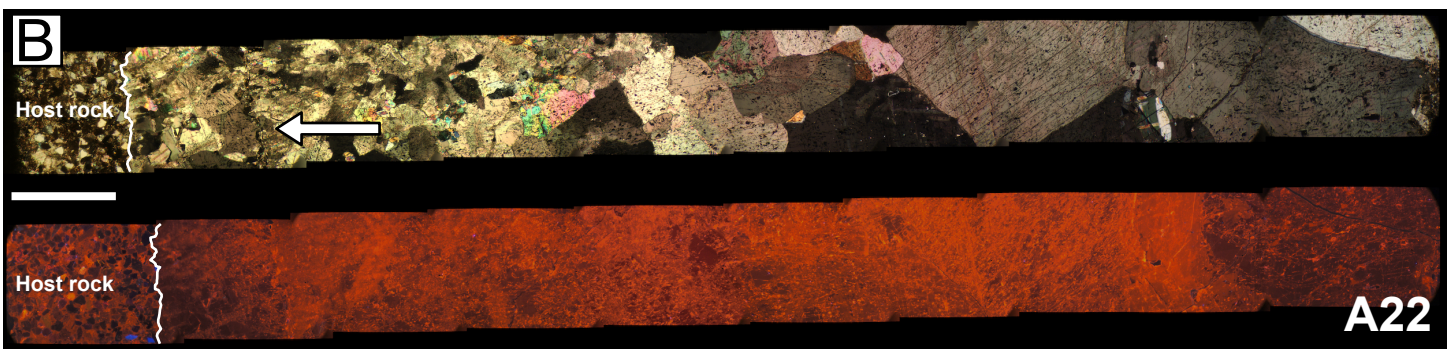
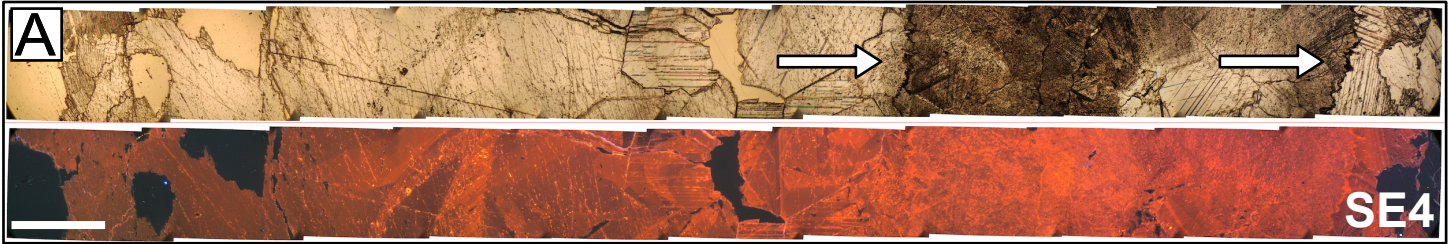
A22

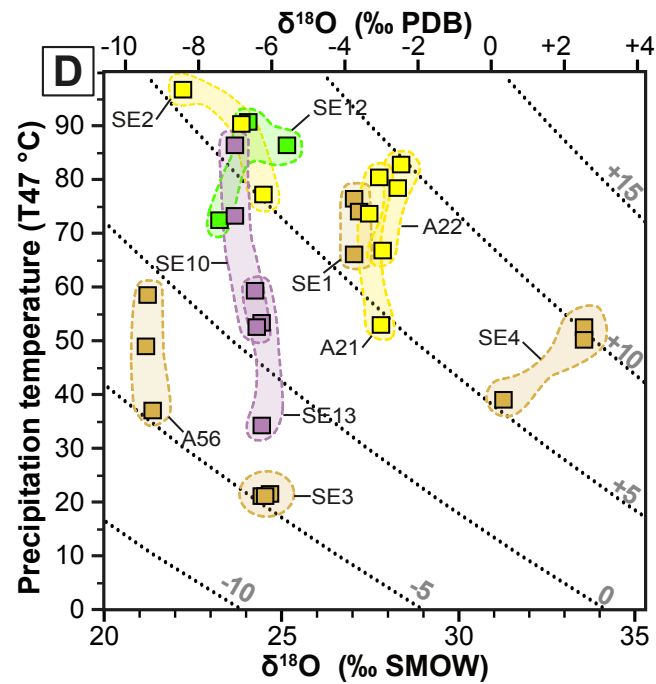
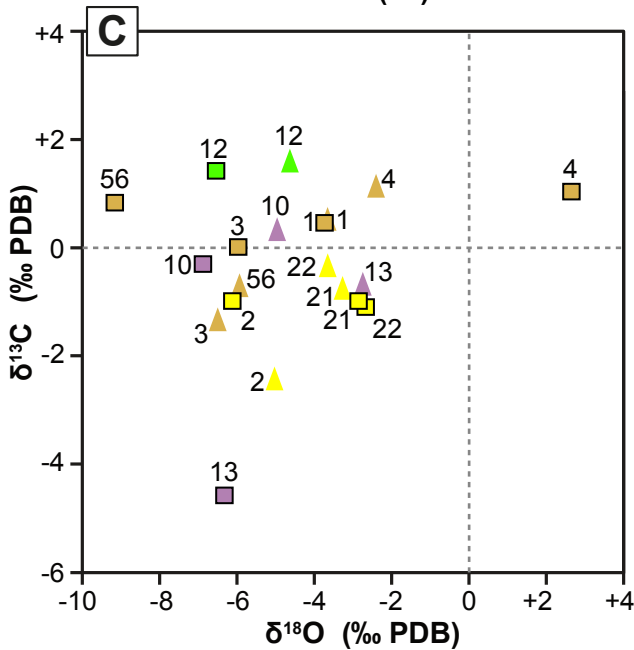
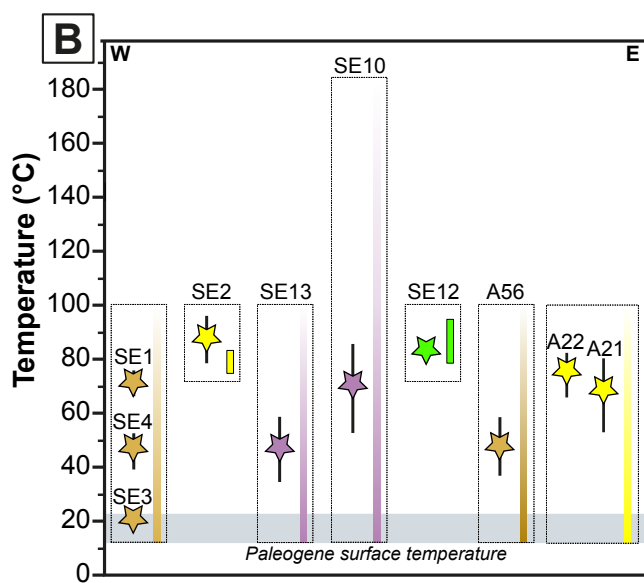
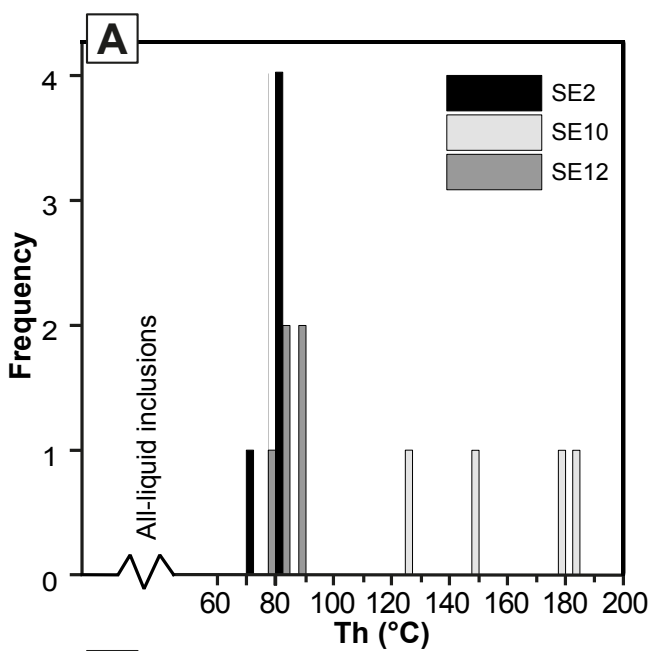


Key









★ T Δ 47 (°C)

▮ Th (°C)

▮ Possible T range
(all-liquid FIs)

▮ Vein

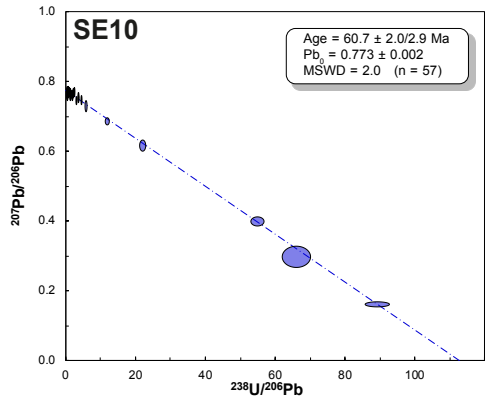
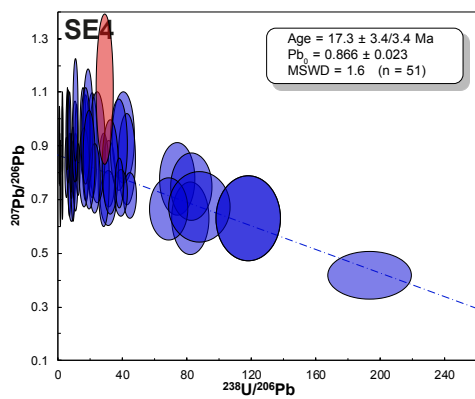
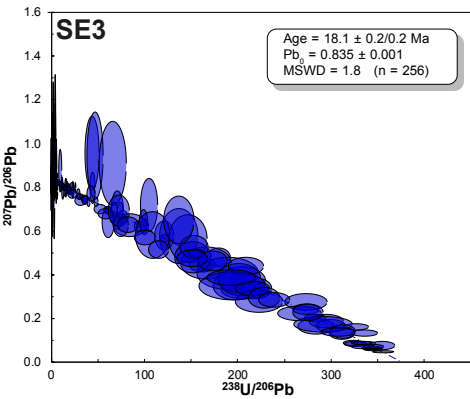
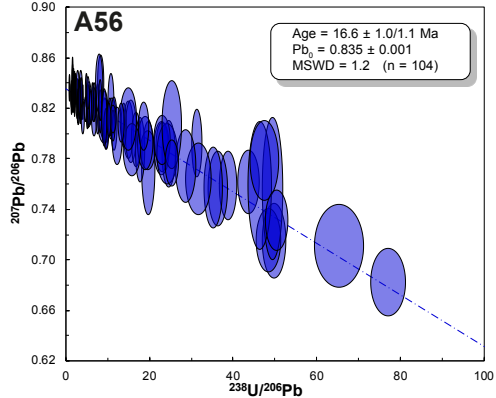
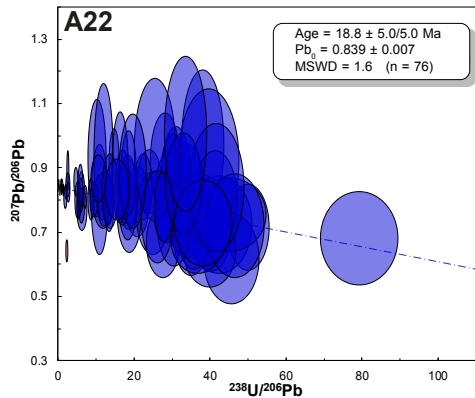
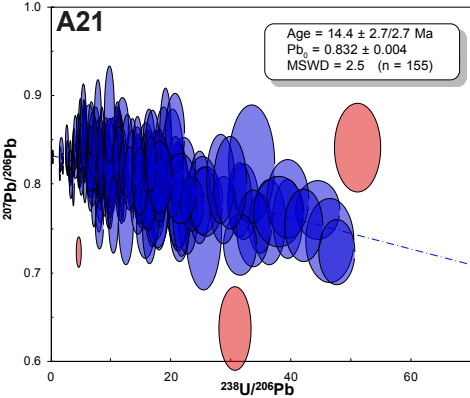
▲ Host rock

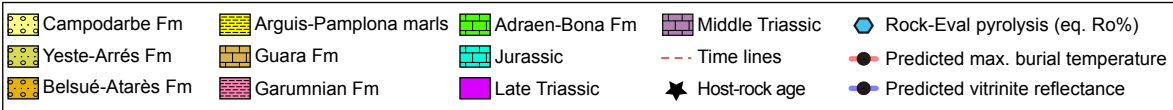
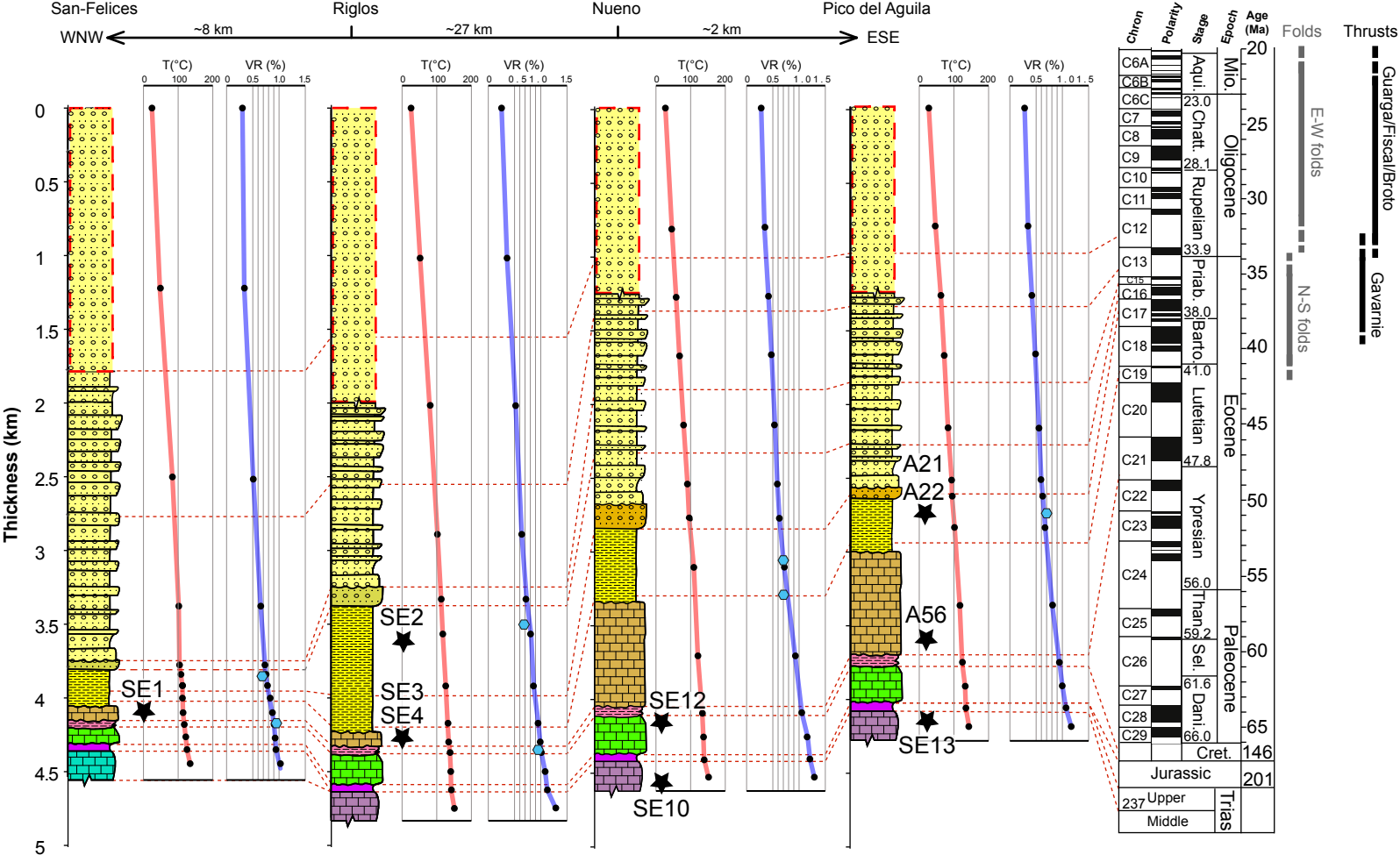
▮ Middle Triassic (Muschelkalk)

▮ Upper Cretaceous (Adraen-Bona Fm)

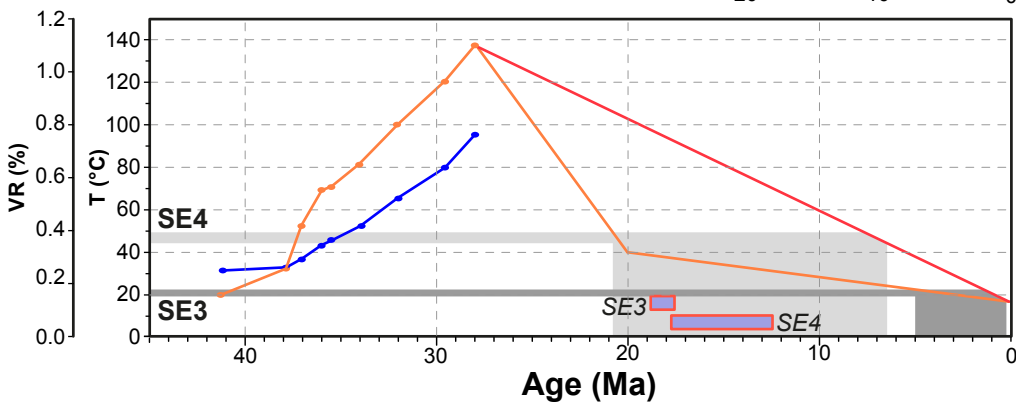
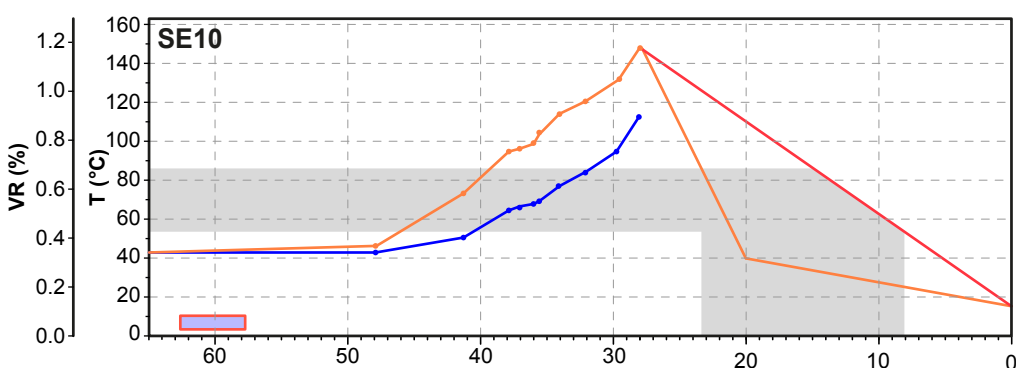
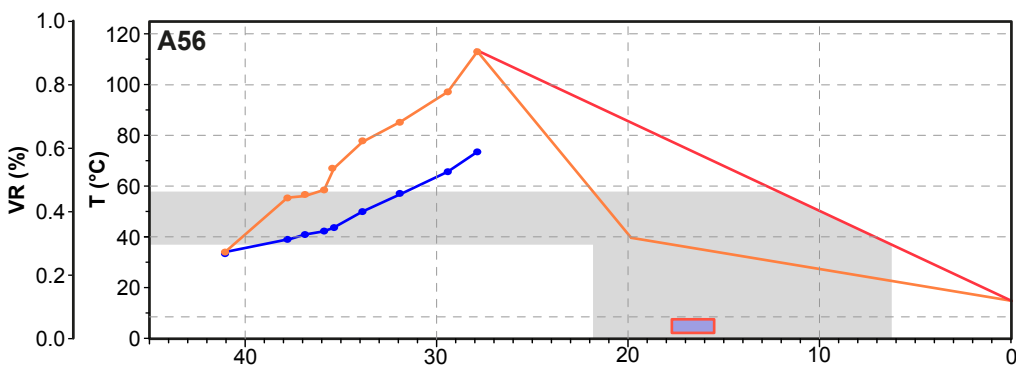
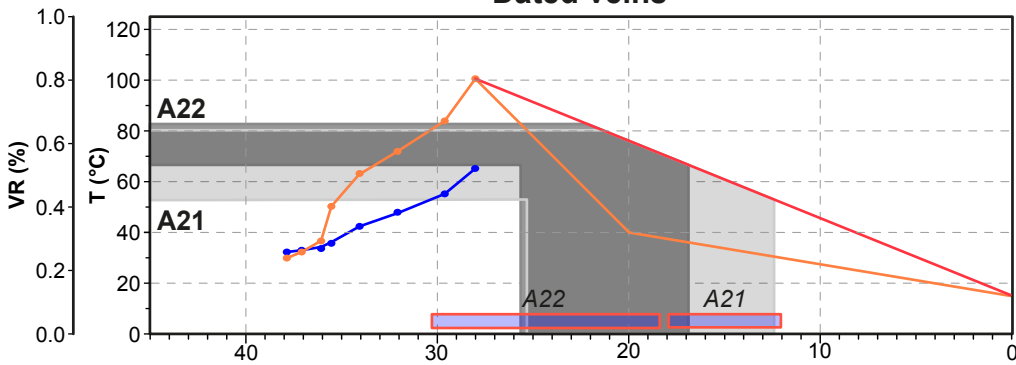
▮ Lutetian (Guara Fm)

▮ Bartonian (Arguis-Pampelona Fm)





Dated veins



Undated veins

